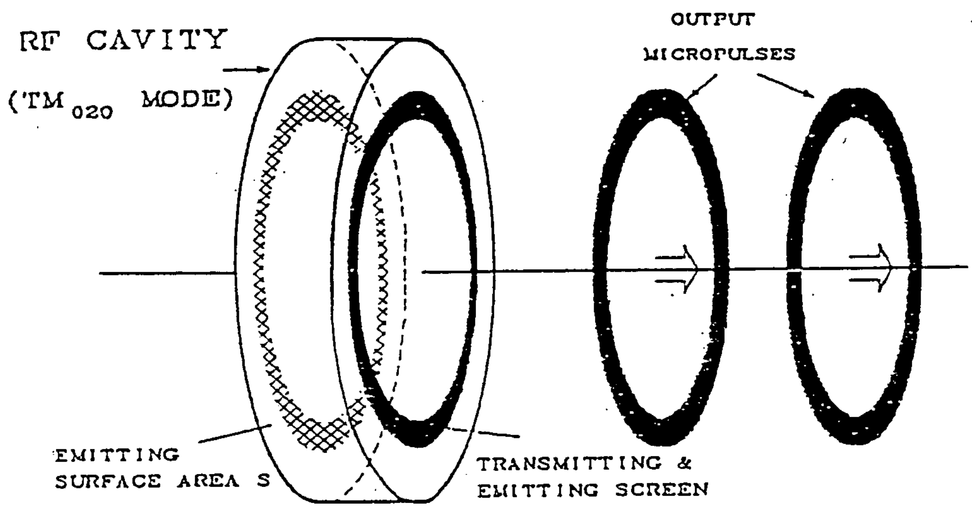

Figure 1: Perspective view of the micropulse gun for a hollow beam in the TM_{020} mode. The inner conductor is not shown.

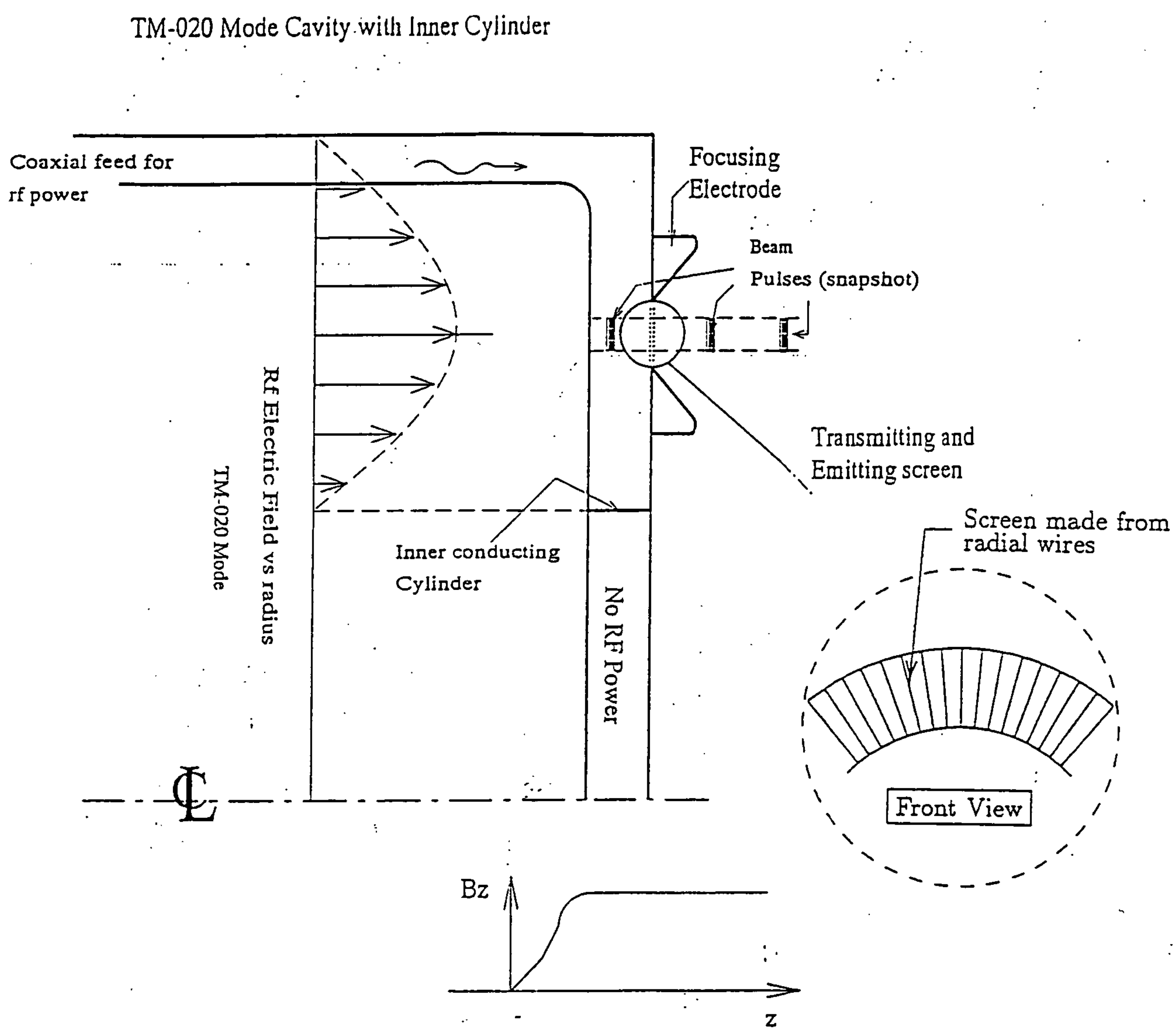

Figure 2: Schematic of rf gun operating in TM_{020} mode.

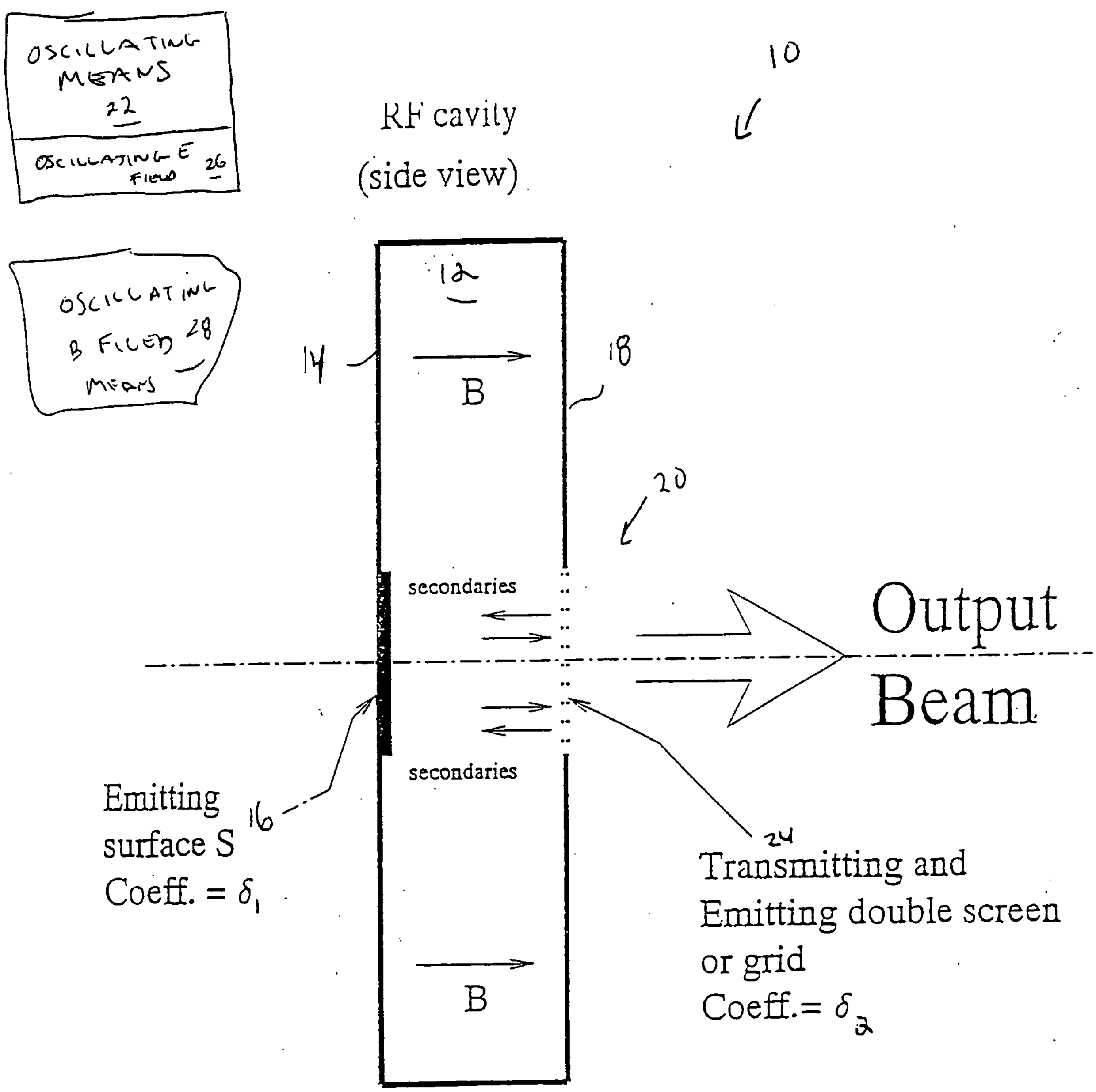

Figure 3: Schematic of micropulse gun for solid beam (TM_{010}) mode. A coaxial feed is used for rf input (not shown).

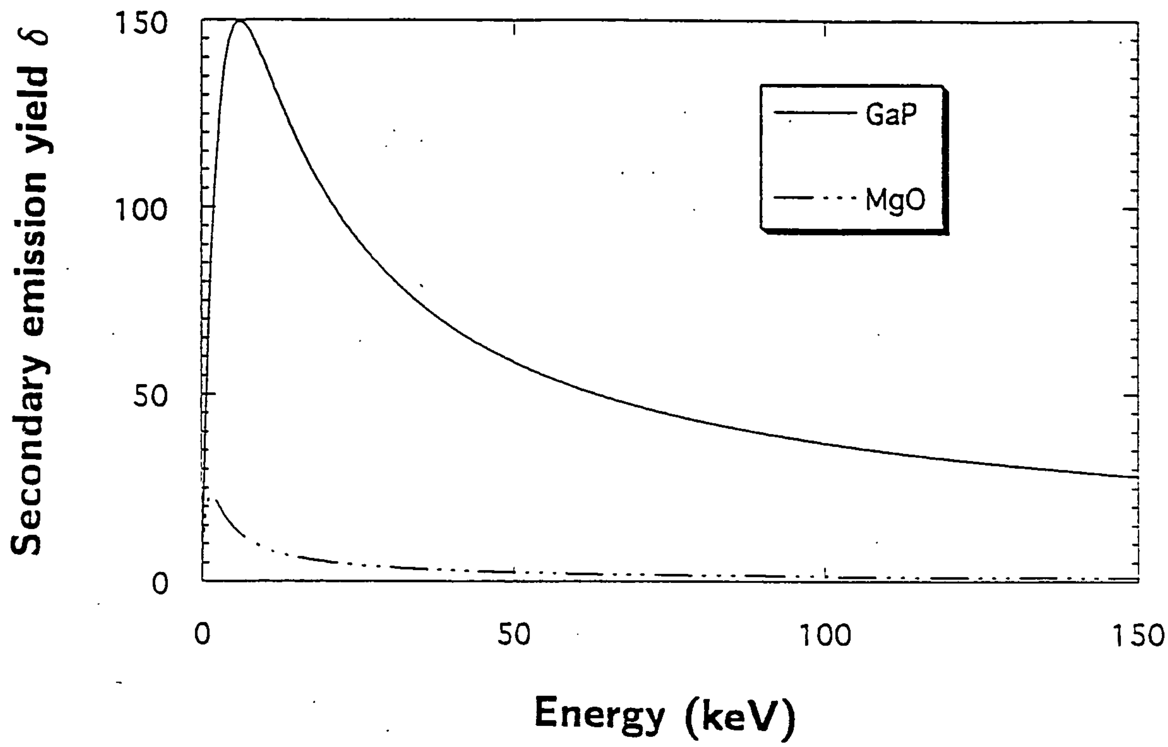

Figure 4: Secondary electron emission yield curve for GaP and MgO

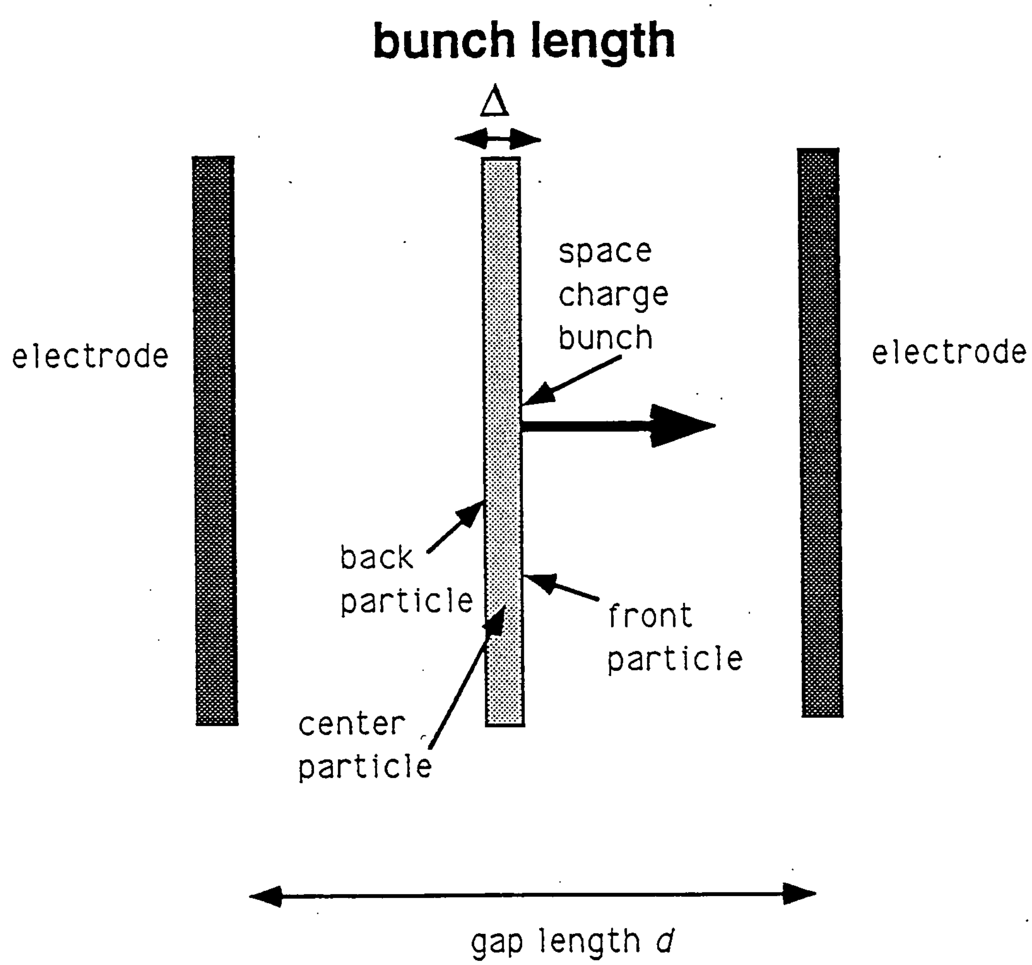

Figure 5: Schematic drawing of model used in theoretical analysis.

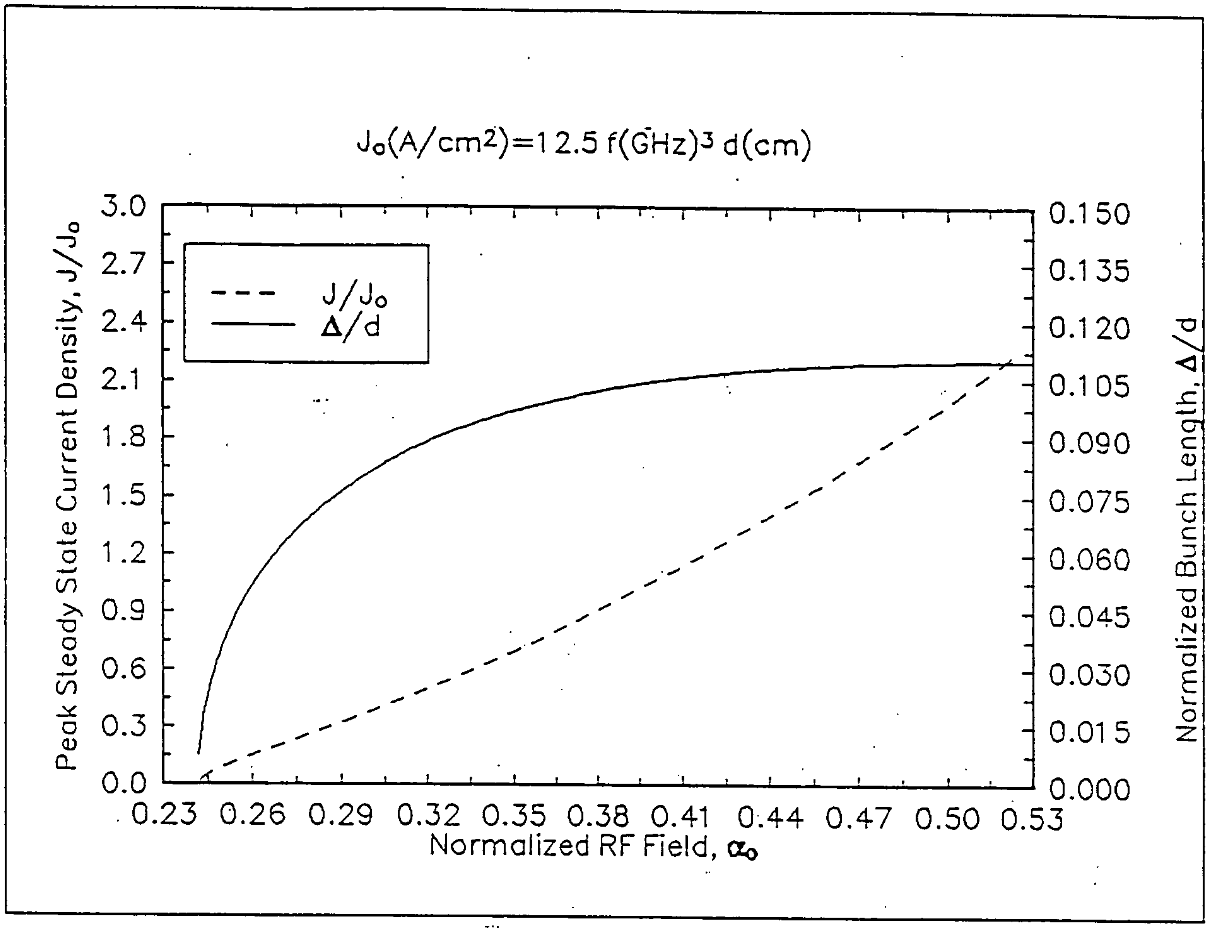

Figure 6: Steady-state current density and bunch length vs. rf field, all parameters are normalized.

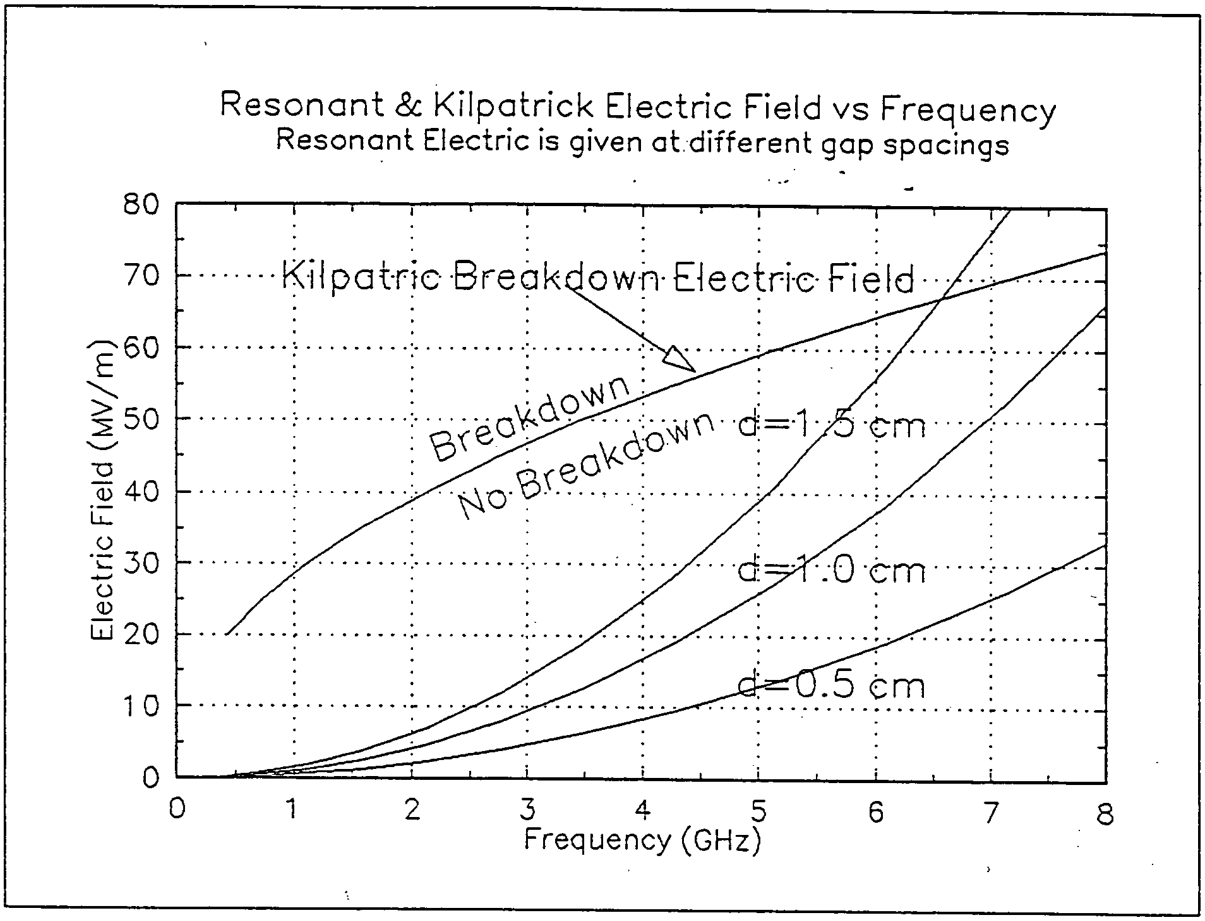

Figure 7: Plot of resonant electric fields for $\alpha_0 = 0.453$ and various gap spacings. Also shown is the critical Kilpatrick electric field as a function of rf frequency.

1.3 GHz, xy plot

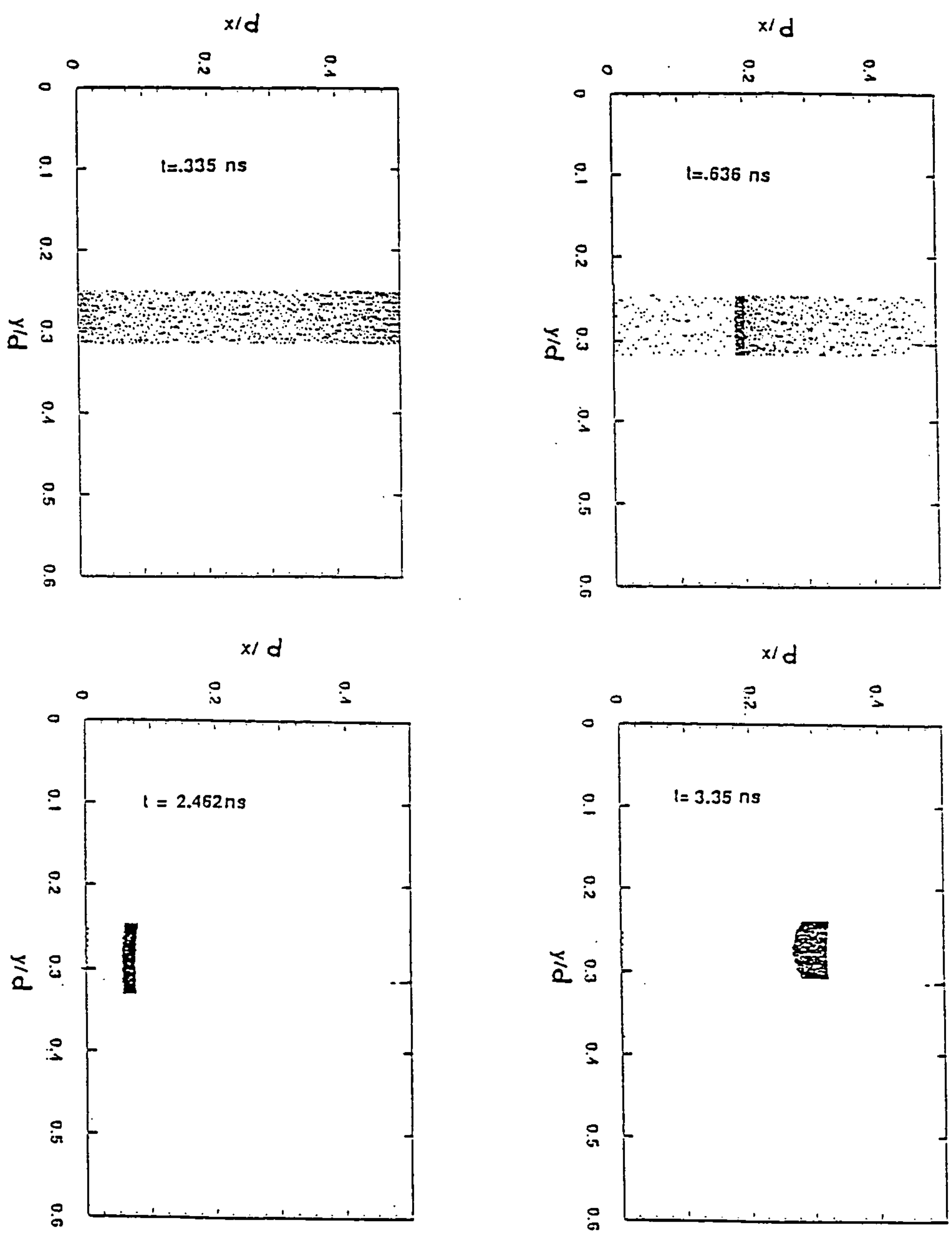

Figure 8: Series of time "snapshots" for a 1.3 GHz, $d = 0.5$ cm cavity using the two-dimensional PIC code with secondary emission. Note the rapid particle build-up and bunching by phase selection. Electrons traverse the horizontal axis. On the vertical axis emission is limited to the region 0.25 to 0.32 cm.

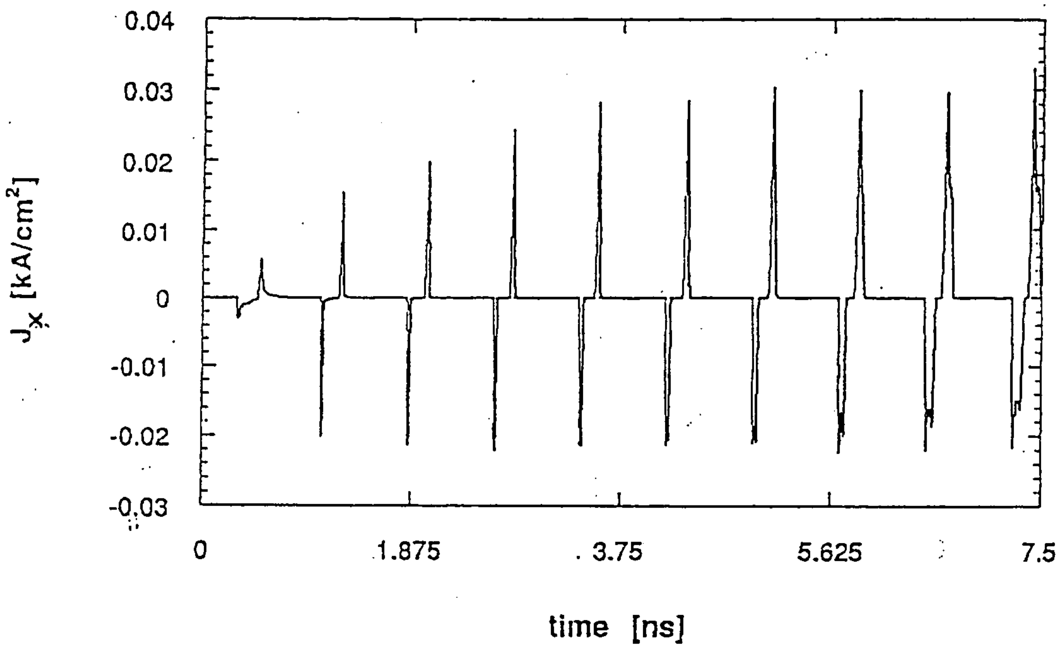

Figure 9: Plot of current density vs. time for simulation with rf frequency 1.3 GHz, voltage amplitude 4.3 kV, $d = 0.5$ cm, and α_0 =0.453.

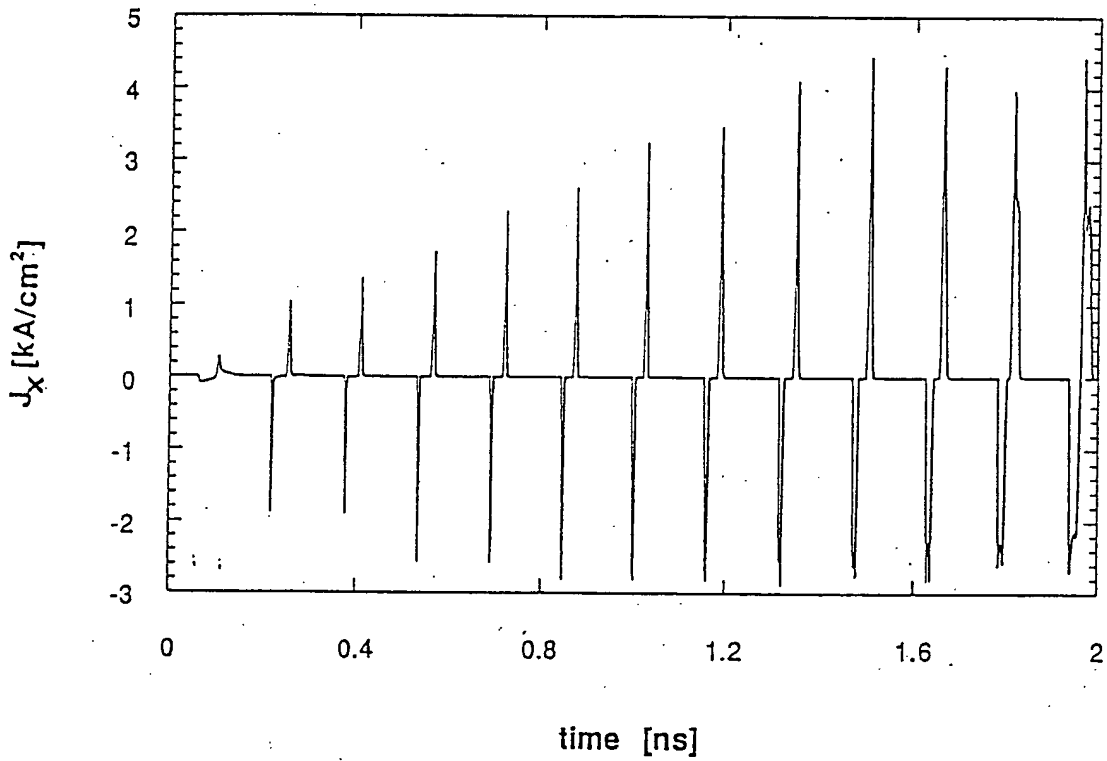

Figure 10: Plot of current density vs. time for simulation with rf frequency 6.4 GHz, voltage amplitude 105 kV, $d = 0.5$ cm, and α_0 =0.453.

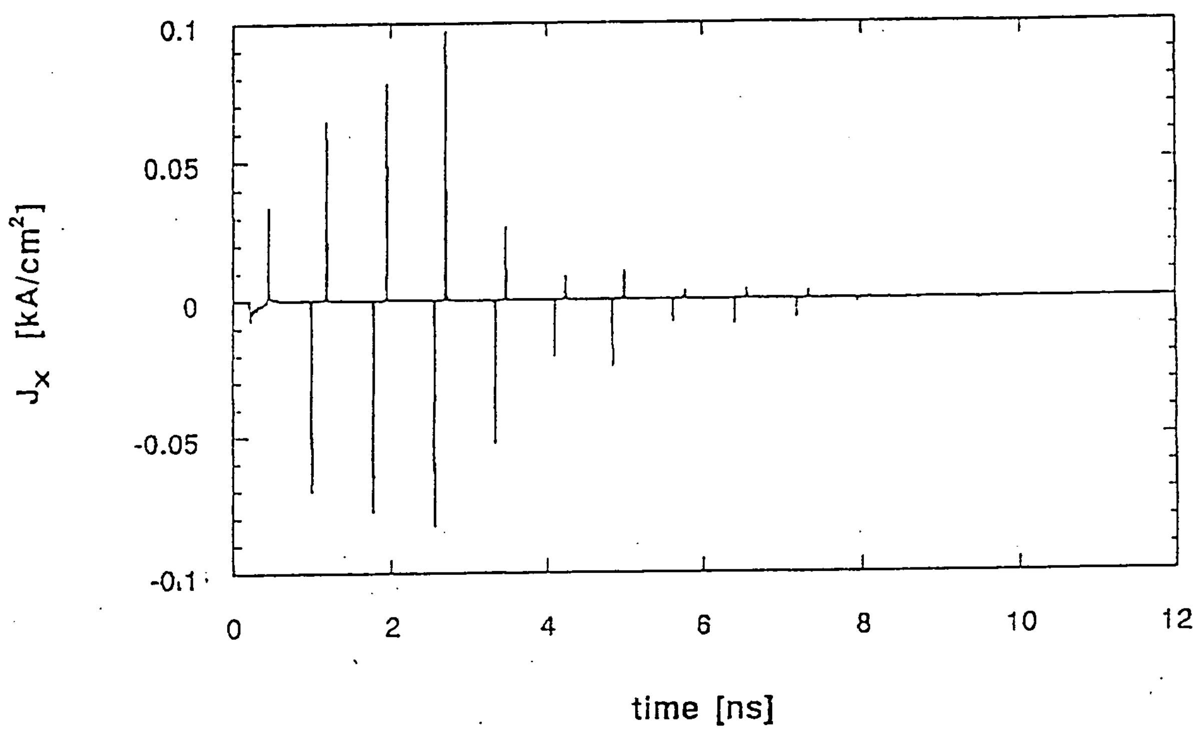

Figure 11: Current density in kA/cm^2 for an off-resonance $d = 0.5$ cm cavity with frequency 1.3 GHz and higher voltage 9.8 kV. Note that not only does current amplification not occur, but the steady-state current is zero.

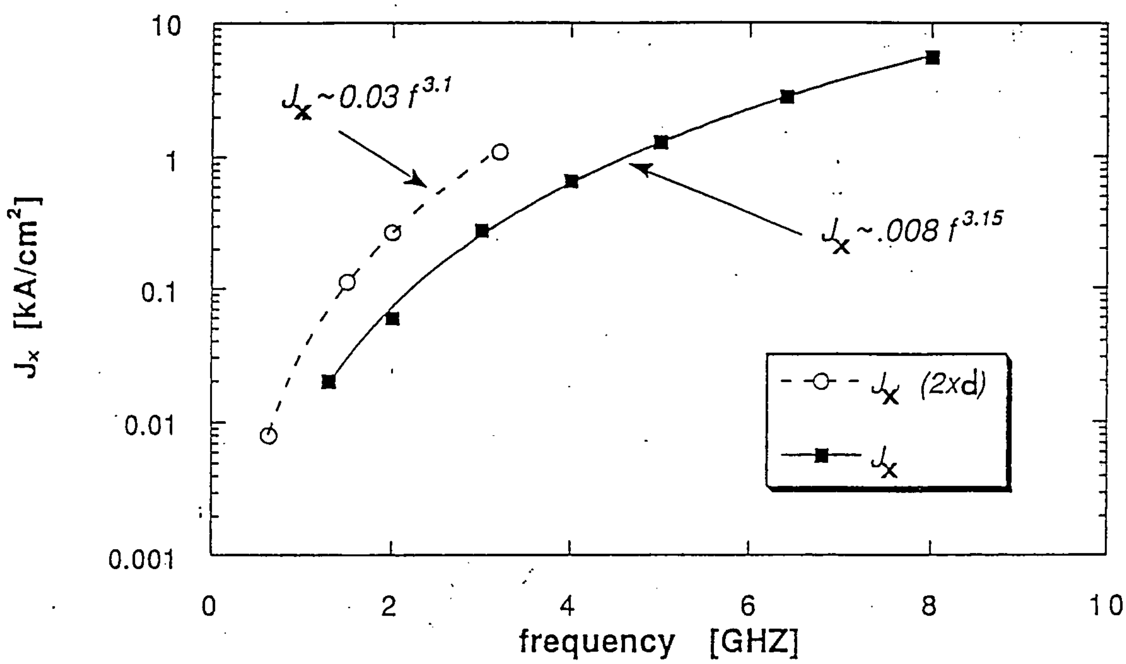

Figure 12: Steady-state current density vs. rf frequency for cavity with α_0 =0.453 and gap lengths of (a) 0.5 cm (solid line) and (b) 1.0 cm (dashed line)

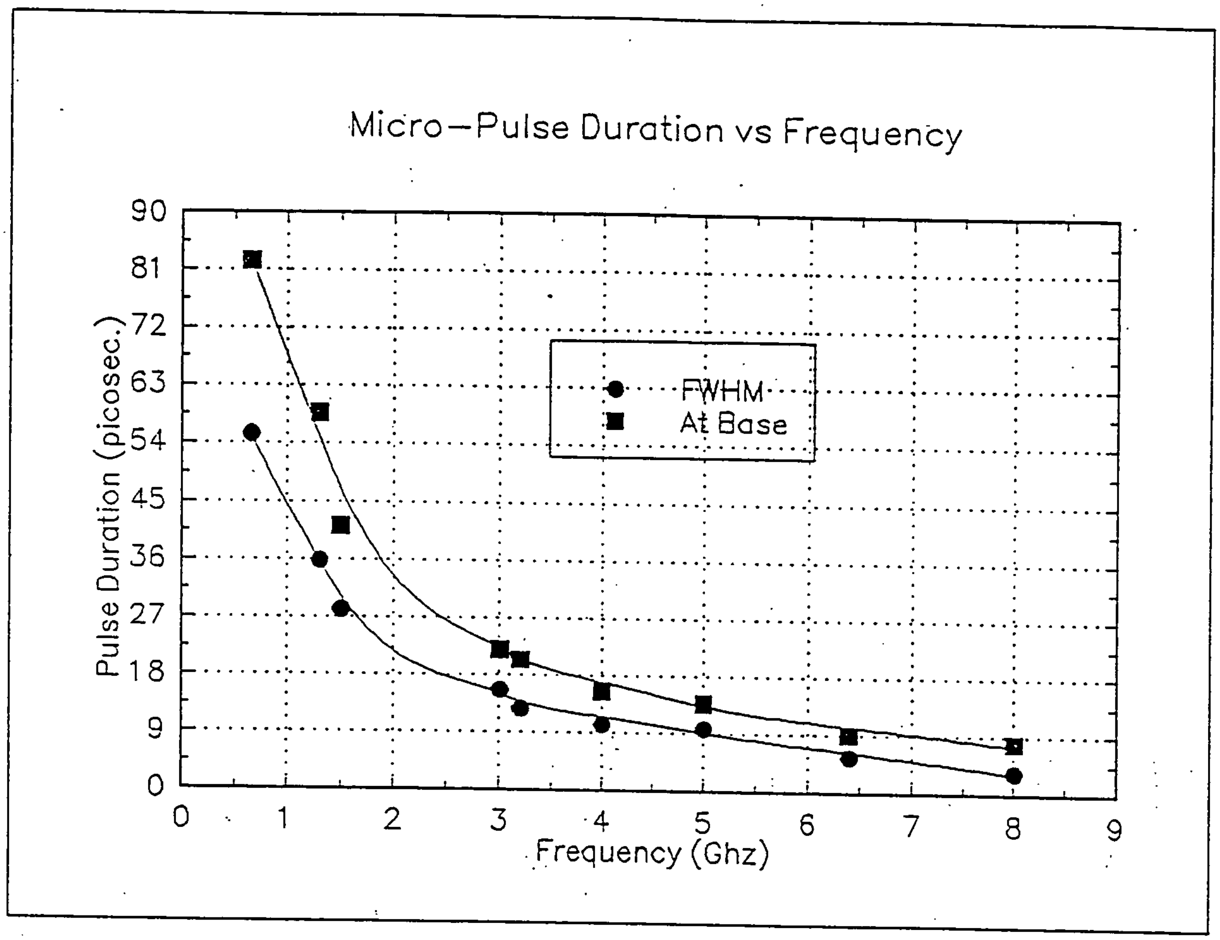

Figure 13: Micro-pulse duration vs. frequency for α_0 =0.453.

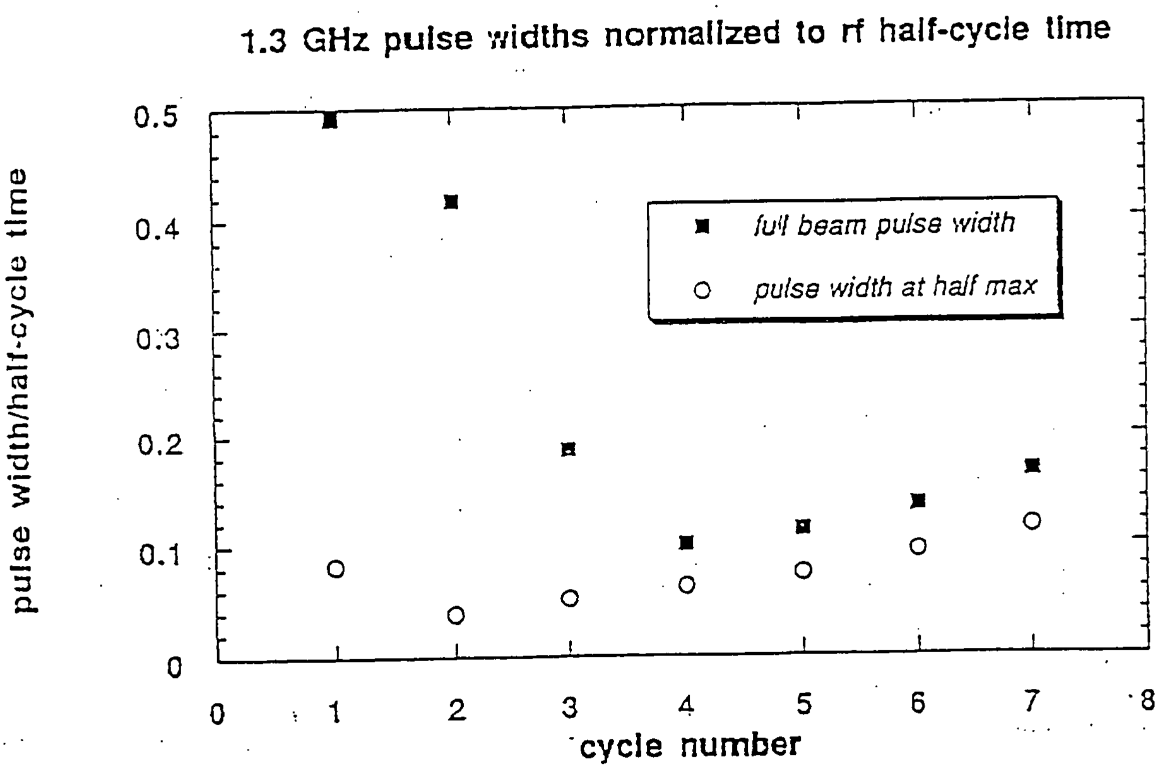

Figure 14: Micro-pulse width (as a fraction of the half-cycle) vs. rf cycle number near the output grid. The full beam pulse width decreases with time, and reaches a minimum at the fourth rf cycle. After saturation there is a slight increase in pulse-width due to space-charge effects.

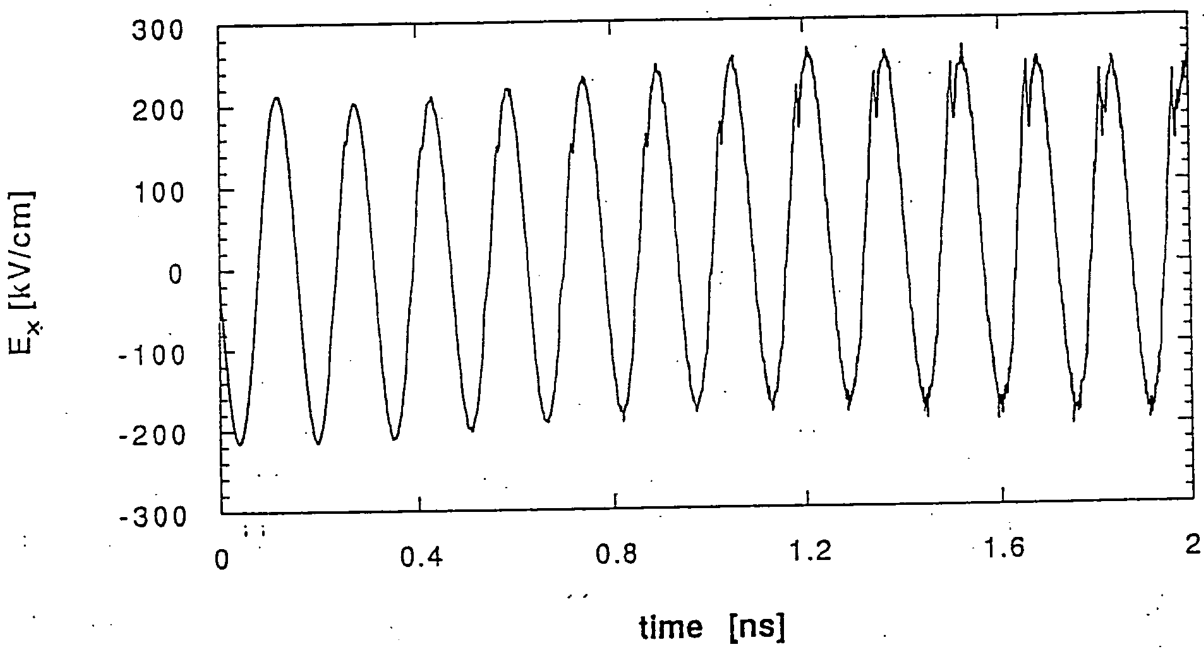

Figure 15: Longitudinal electric field in kv/cm as measured by a probe near the exit grid for the 6.4 GHz, 105 kV simulation.

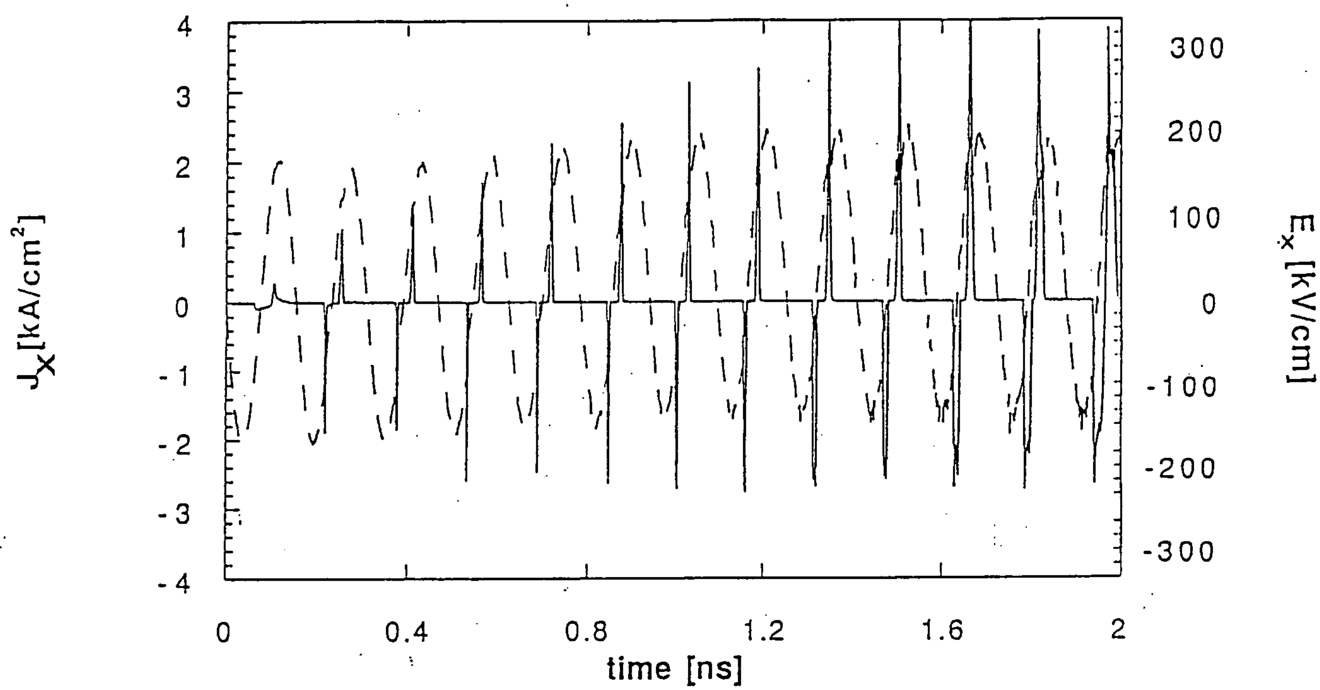

Figure 16: Plot of the current density in kA/cm² [solid line] and the longitudinal electric field [dashed line] for the 6.4 GHz, 105 kV simulation.

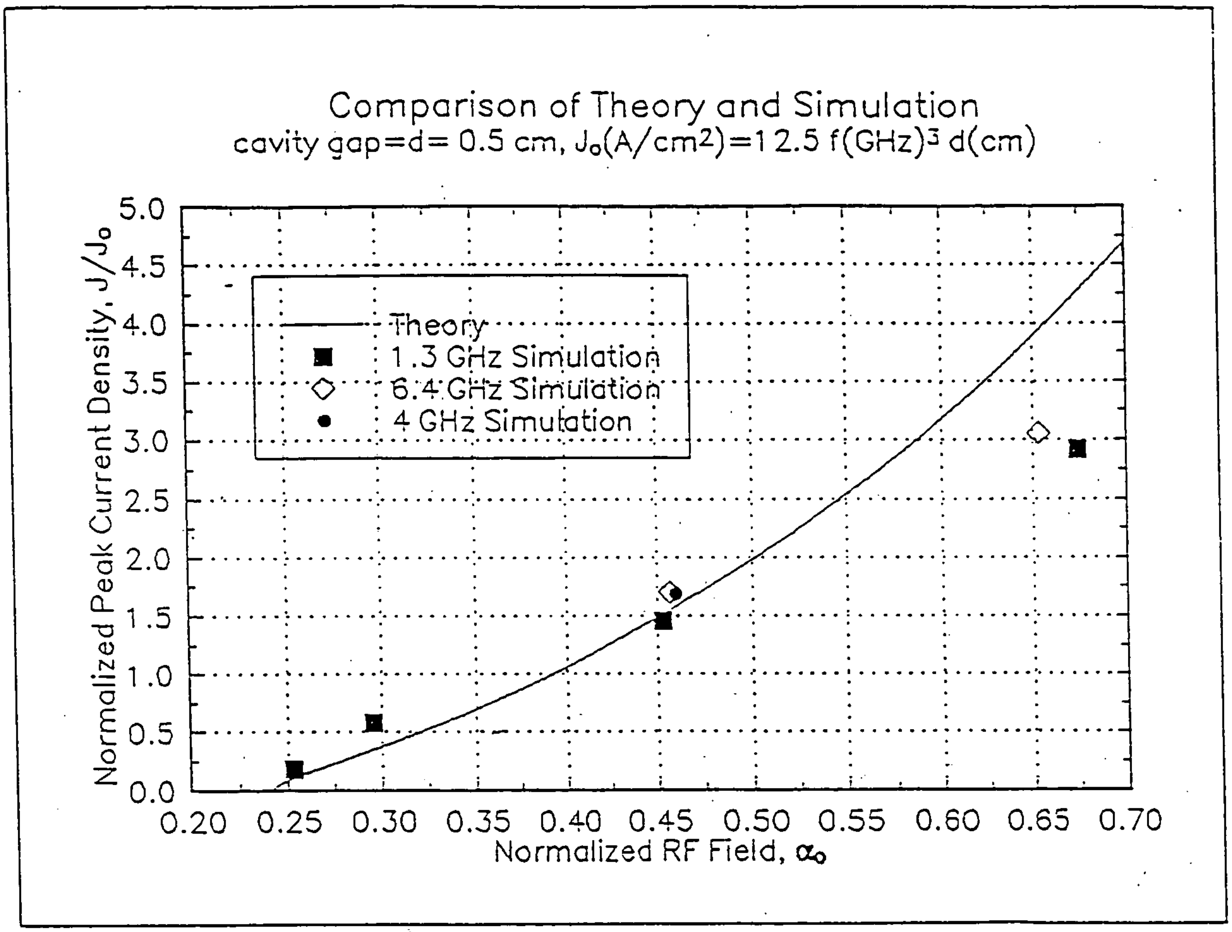

Figure 17: Resonant Tuning Curve (both simulation and theory) showing the tolerance of the micropulse electron gun.

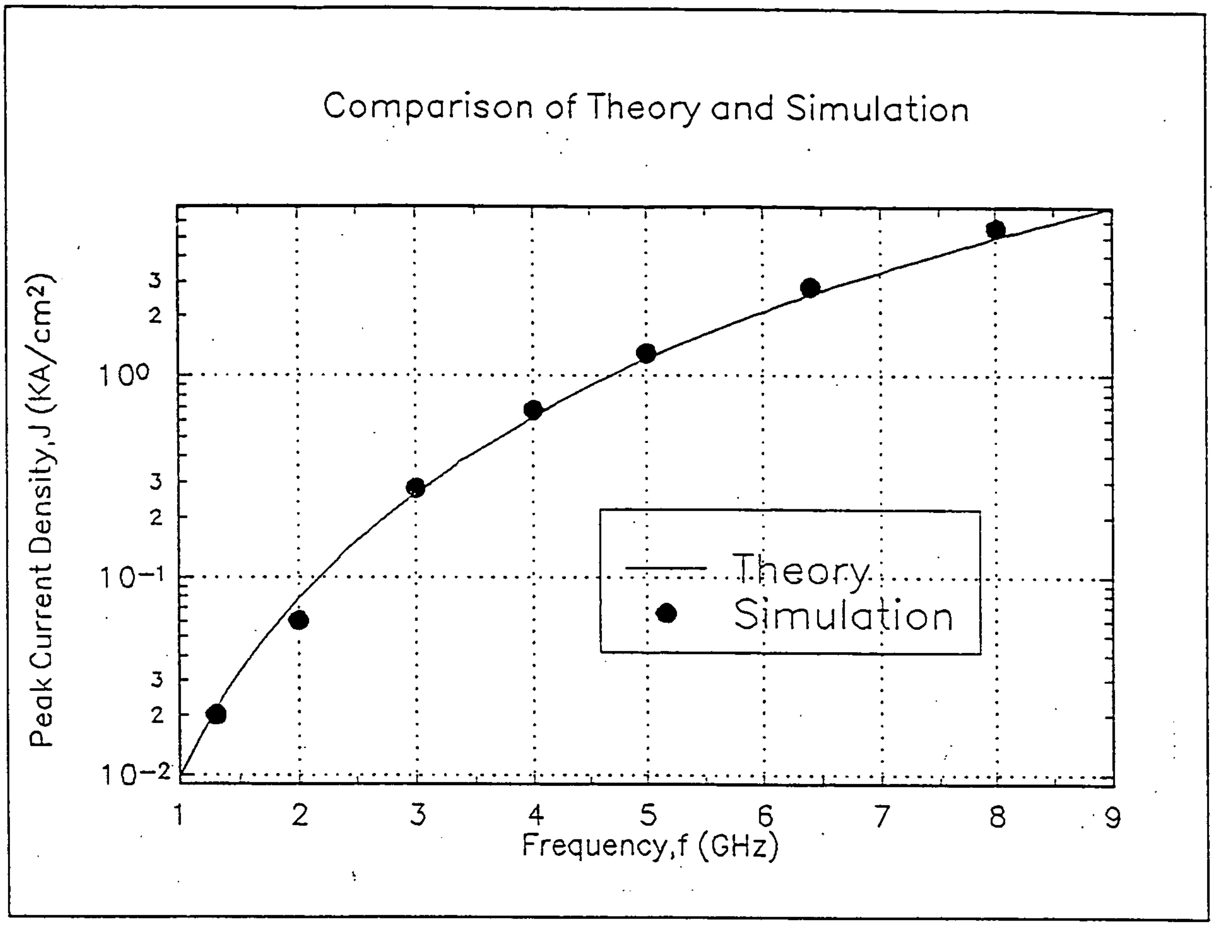

Figure 18: Comparison of peak current density in kA/cm^2 versus frequency for simulation and theory for a gap length of 0.5 cm and drive parameter $\alpha_0 = 0.453$.

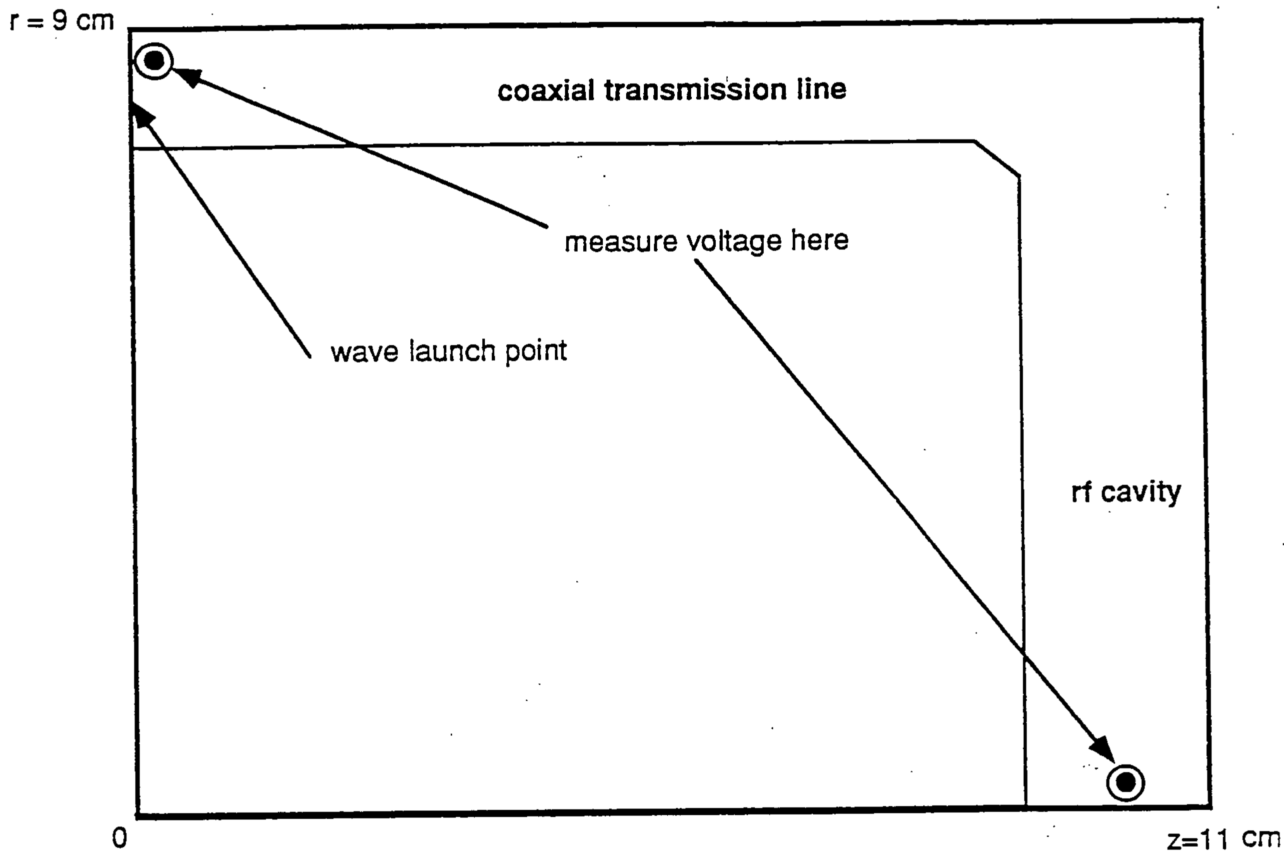

Figure 19: Side view of a cylindrically symmetric coaxial transmission line and cavity. An rf wave is launched at the left end of the coaxial line.

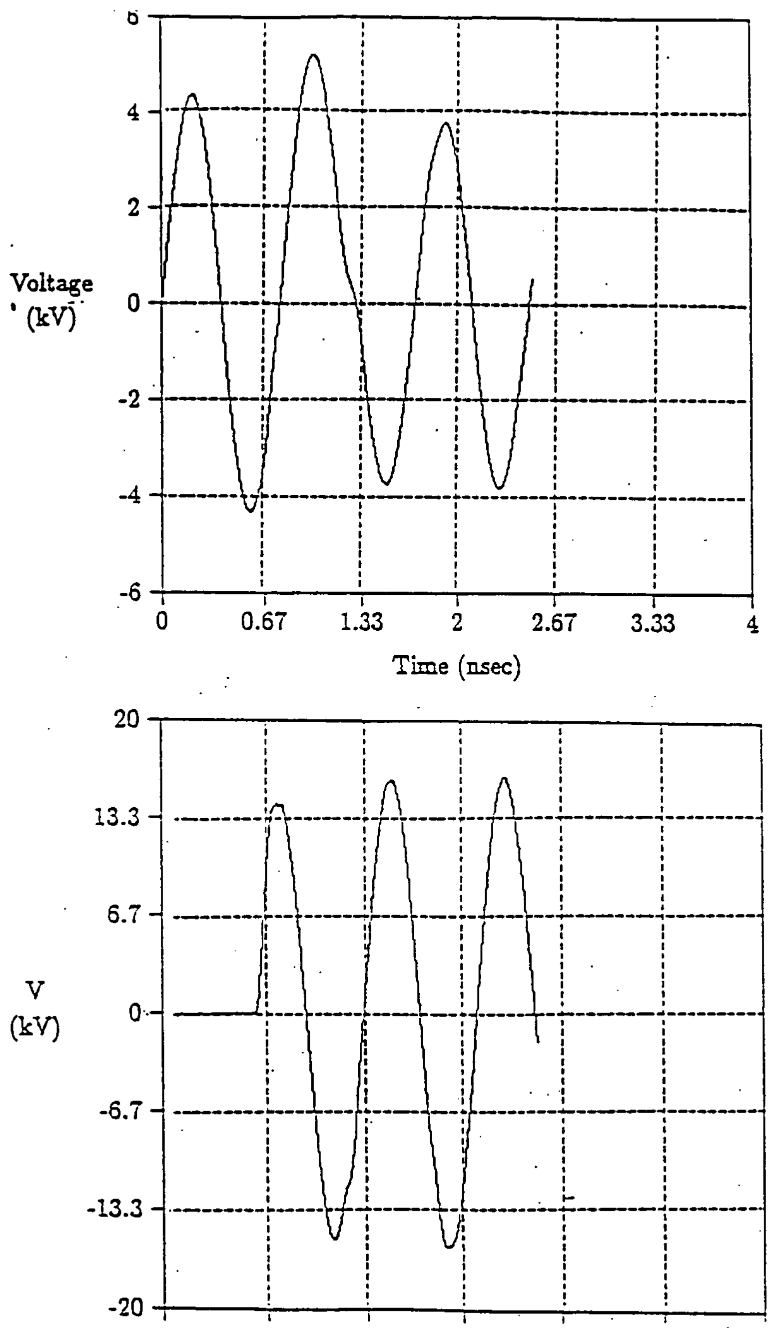

Figure 20: Resulting voltages for a TM_{010} cavity at 1.275 GHz (9 cm radius) with a one cm cavity gap and one cm coaxial gap. (top) voltage measured at entrance of coax, and (bottom) voltage measured at cavity center.

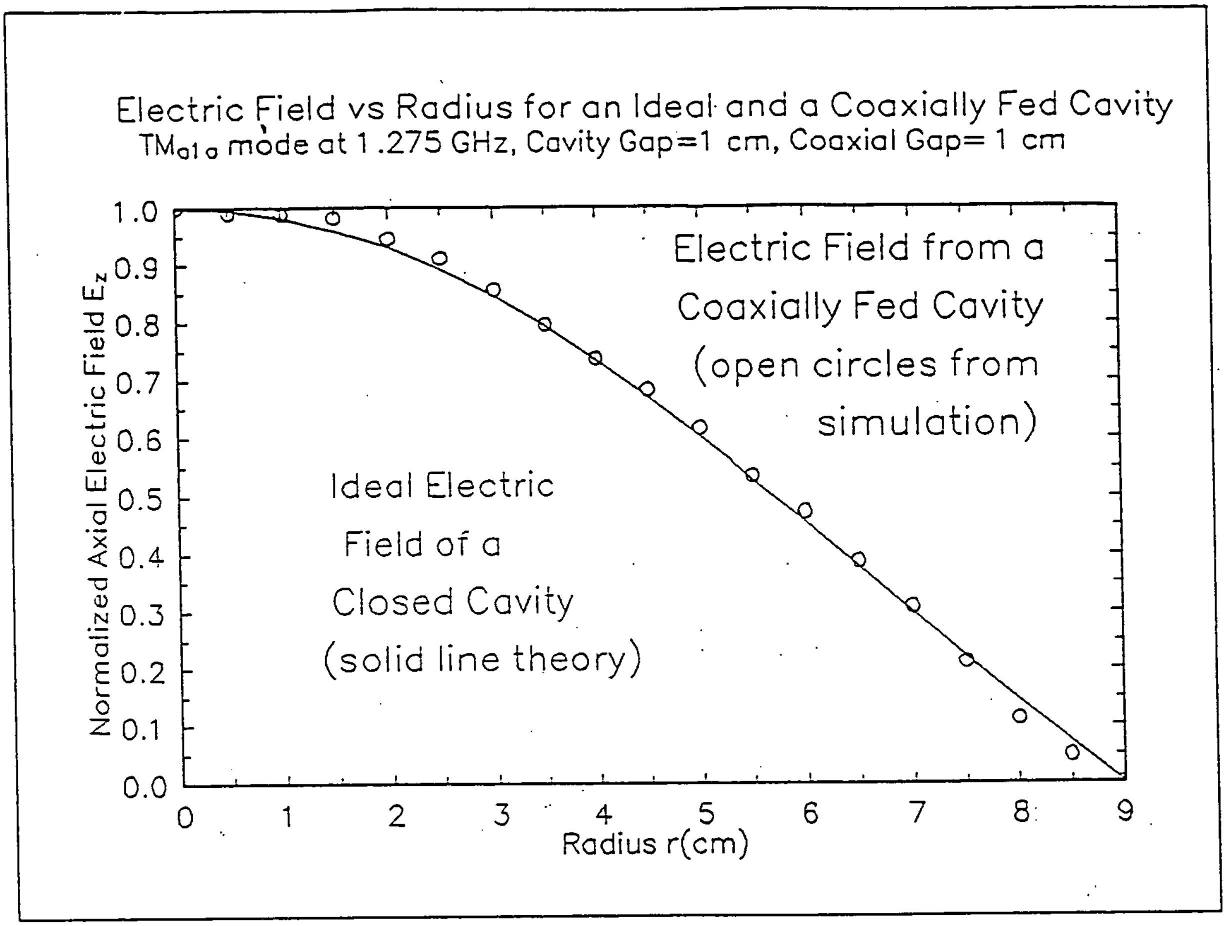

Figure 21: Electric field from a coaxially fed cavity (TM_{010} mode) showing simulation values (open circles) and theoretical curve for an ideal closed cavity.

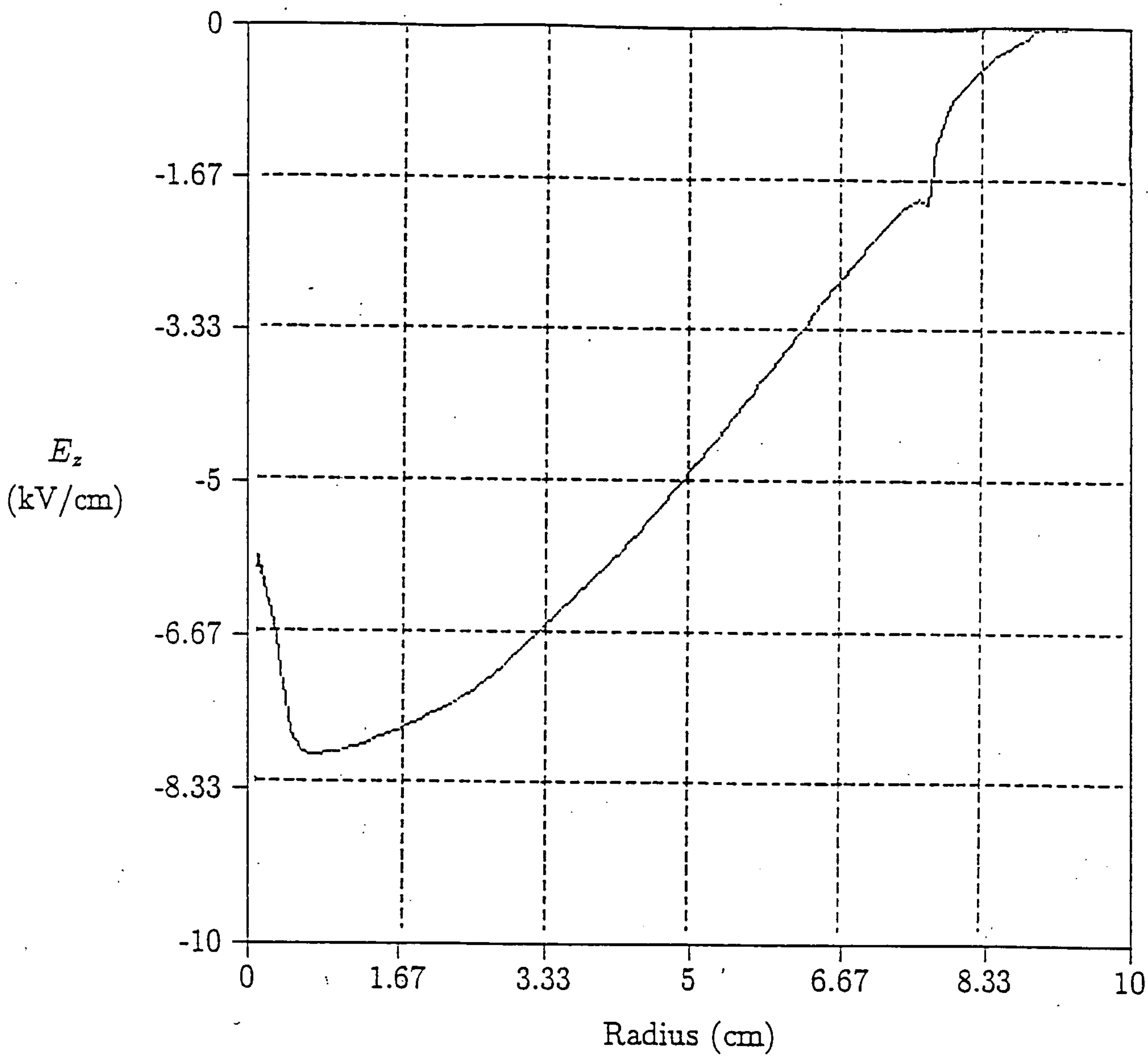

Figure 22: Axial electric field in cavity with a one cm diameter, 40 amp/cm^2, 25 ps long beam emitted into the cavity. The curve is inverted compared to the plot of Fig. 21. However, the depression at $R = 0$ cm due to space charge is clearly seen. Beam loading reduces the field by about 1/3.

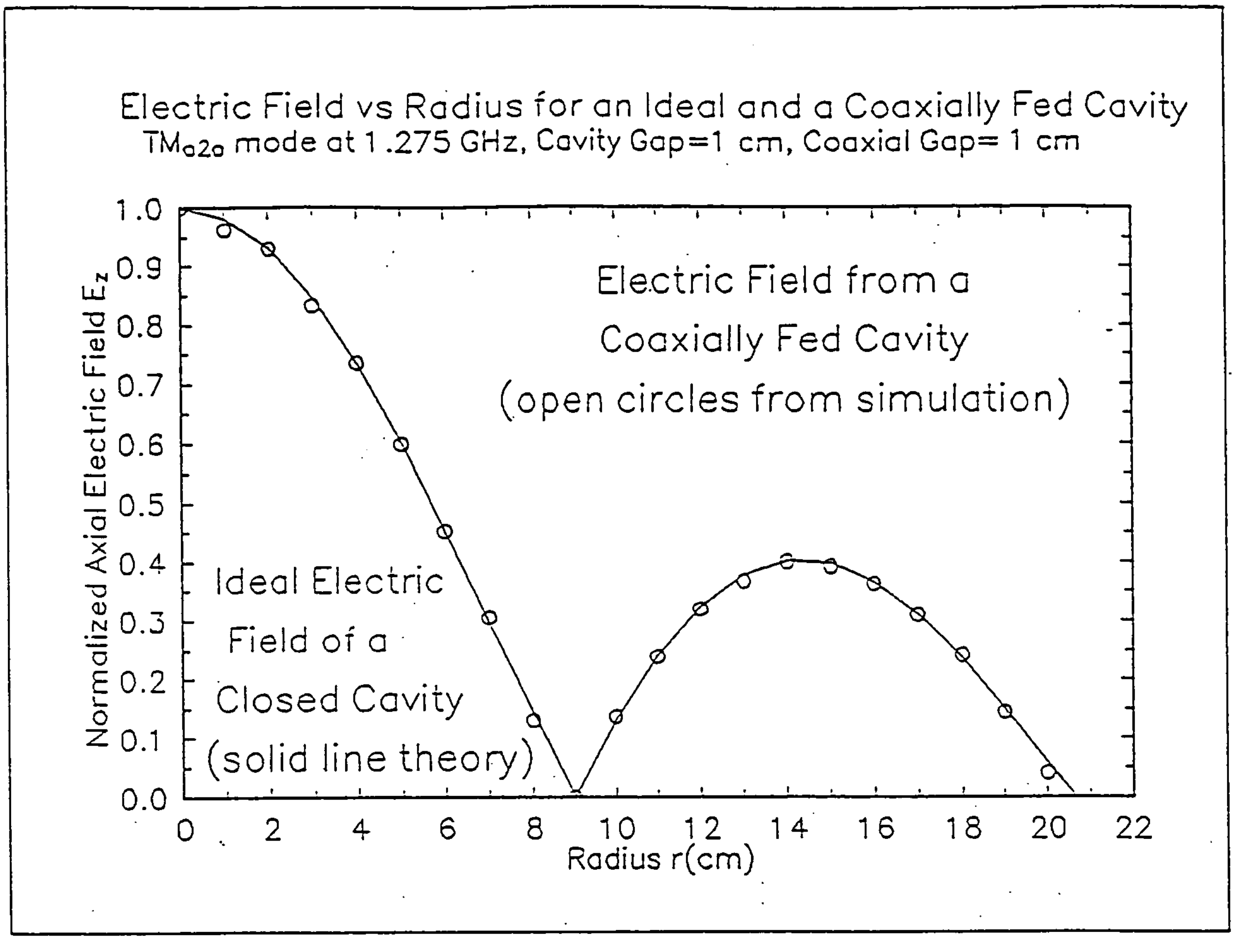

Figure 23: Electric field from a coaxially fed cavity (TM_{020} mode) showing simulation values (open circles) and theoretical curve for an ideal closed cavity.

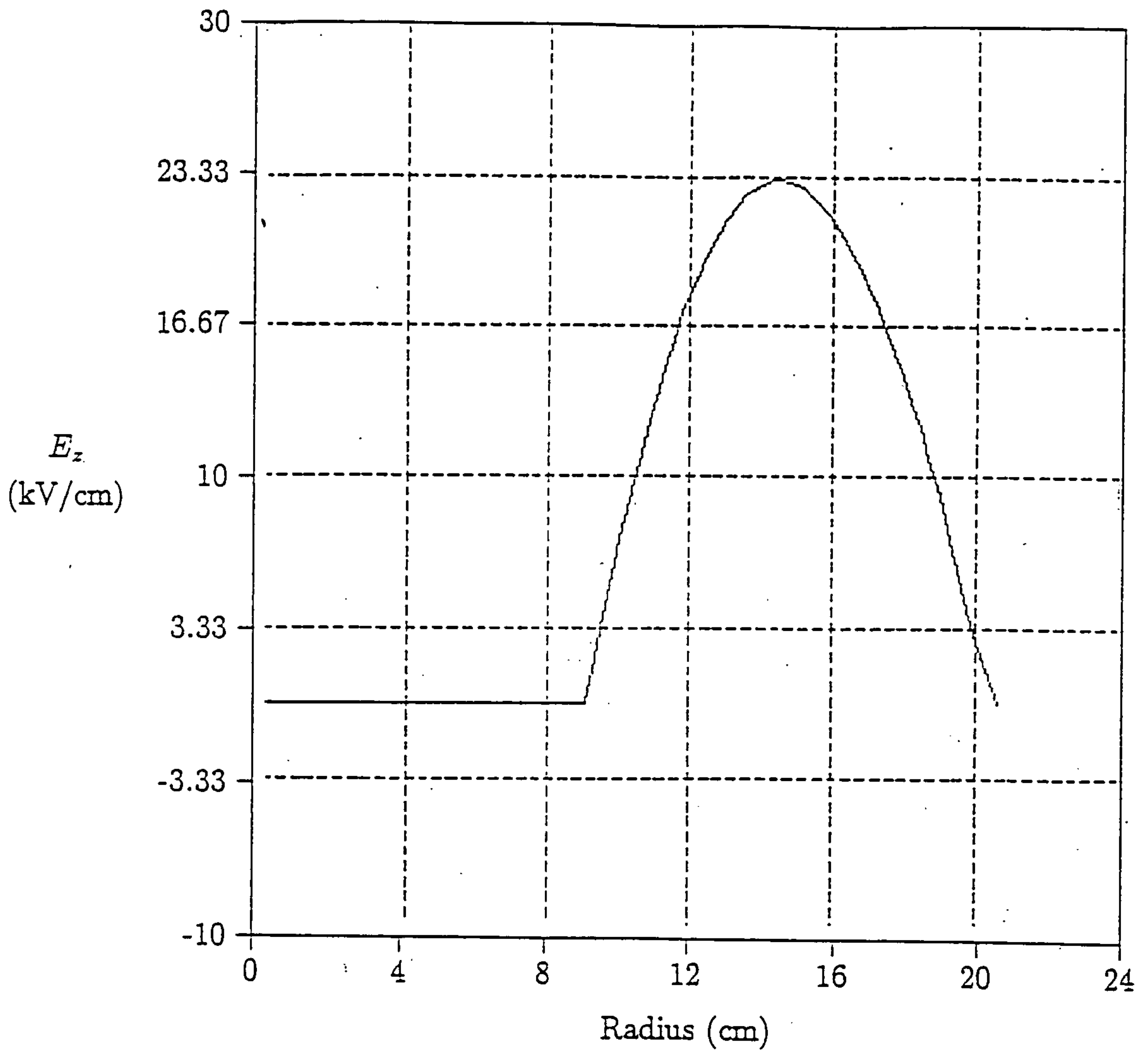

Figure 24: Axial electric field vs. radius from a coaxially fed cavity (TM_{020} mode (simulation) with inner conductor at first zero of the mode. The first peak has clearly been eliminated. Frequency 1.275 GHz and one cm gap.

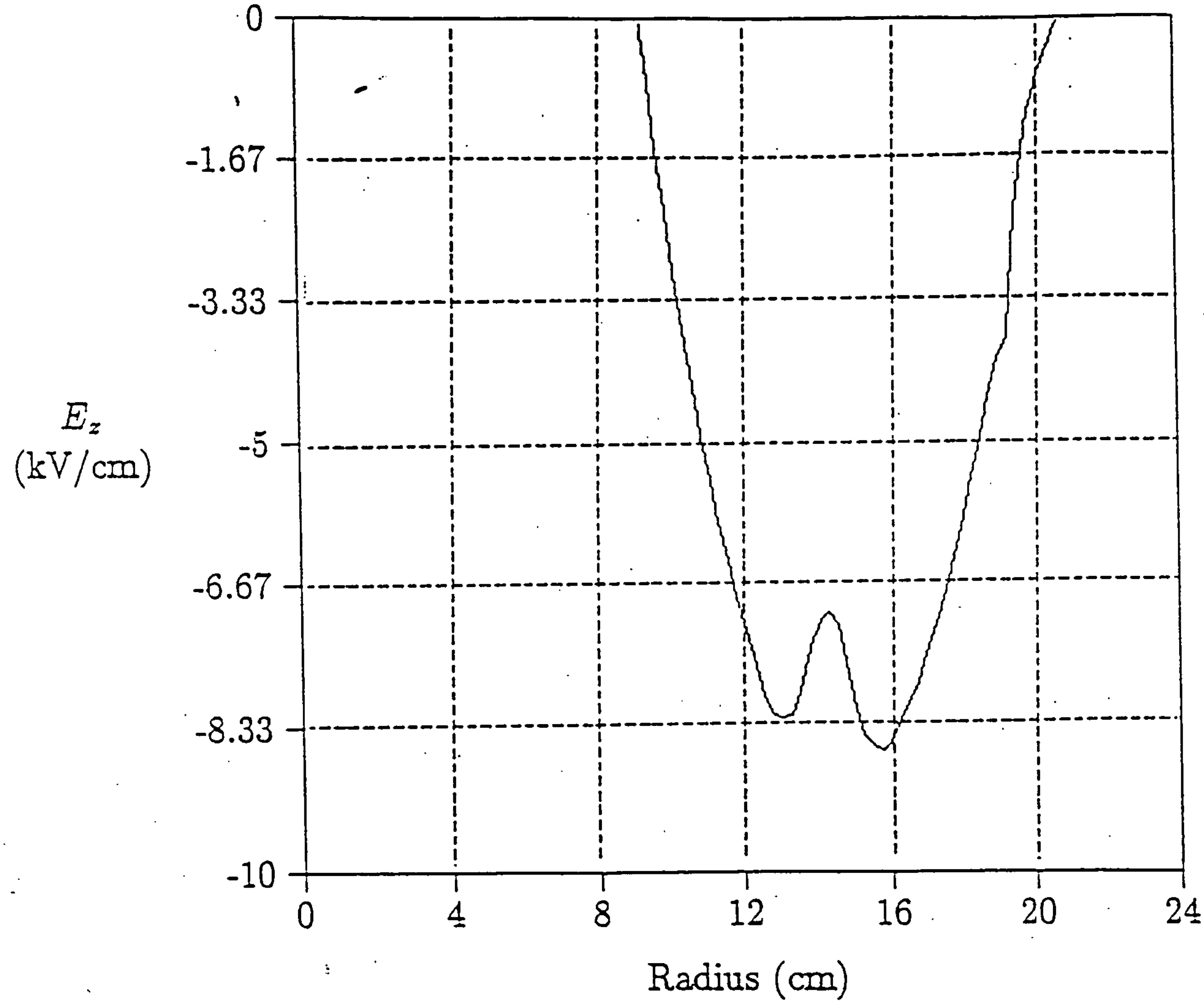

Figure 25: Axial electric field as a function of radius loaded down by a 40 amp/cm^2, 25 ps pulse, and one cm diameter electron beam. The curve is inverted compared to the plot of Fig. 24. However, the depression at $R \approx 14$ cm due to space charge is clearly seen.

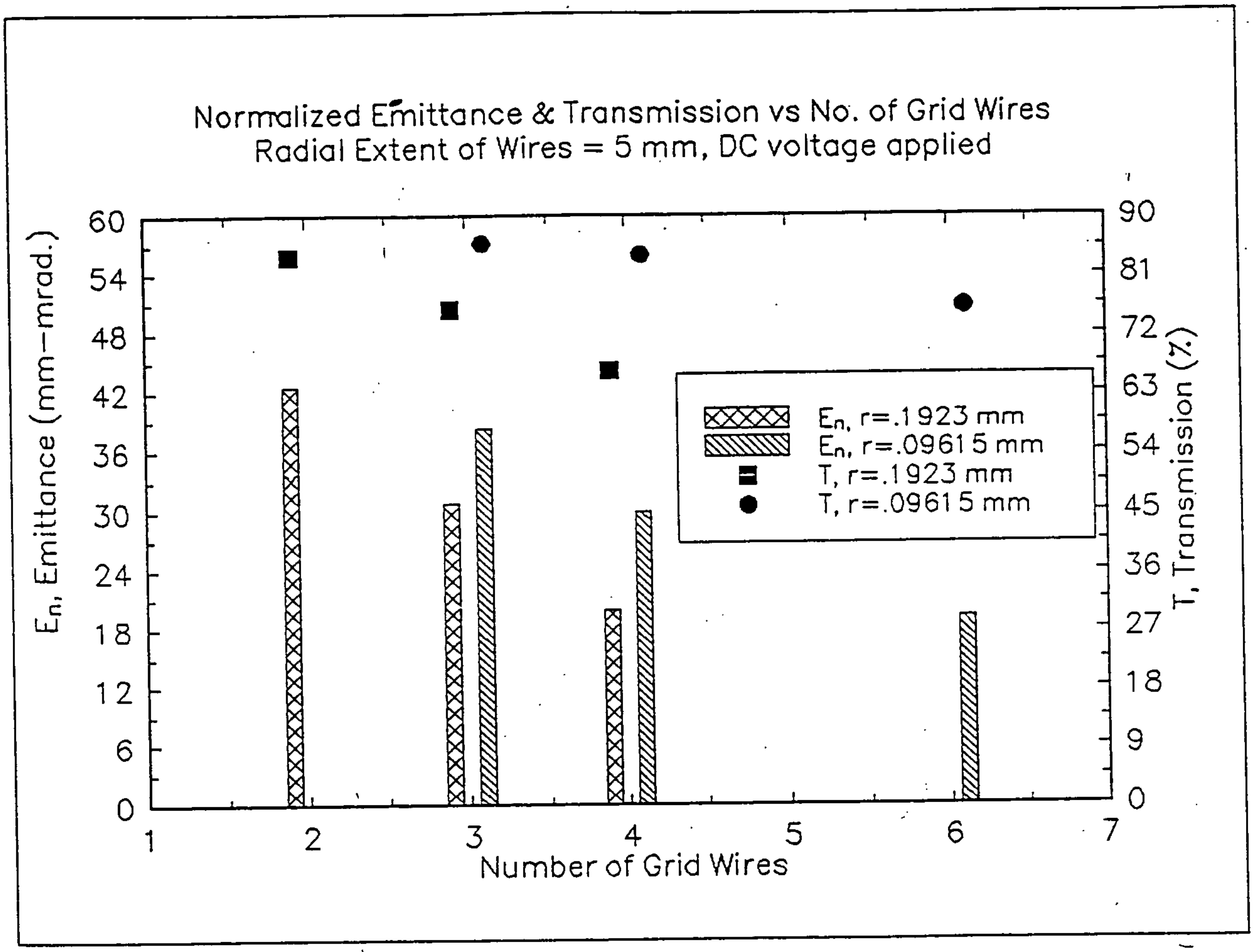

Figure 26: Normalized emmitance and transmission versus number of grid wires with a dc voltage applied to the cavity.

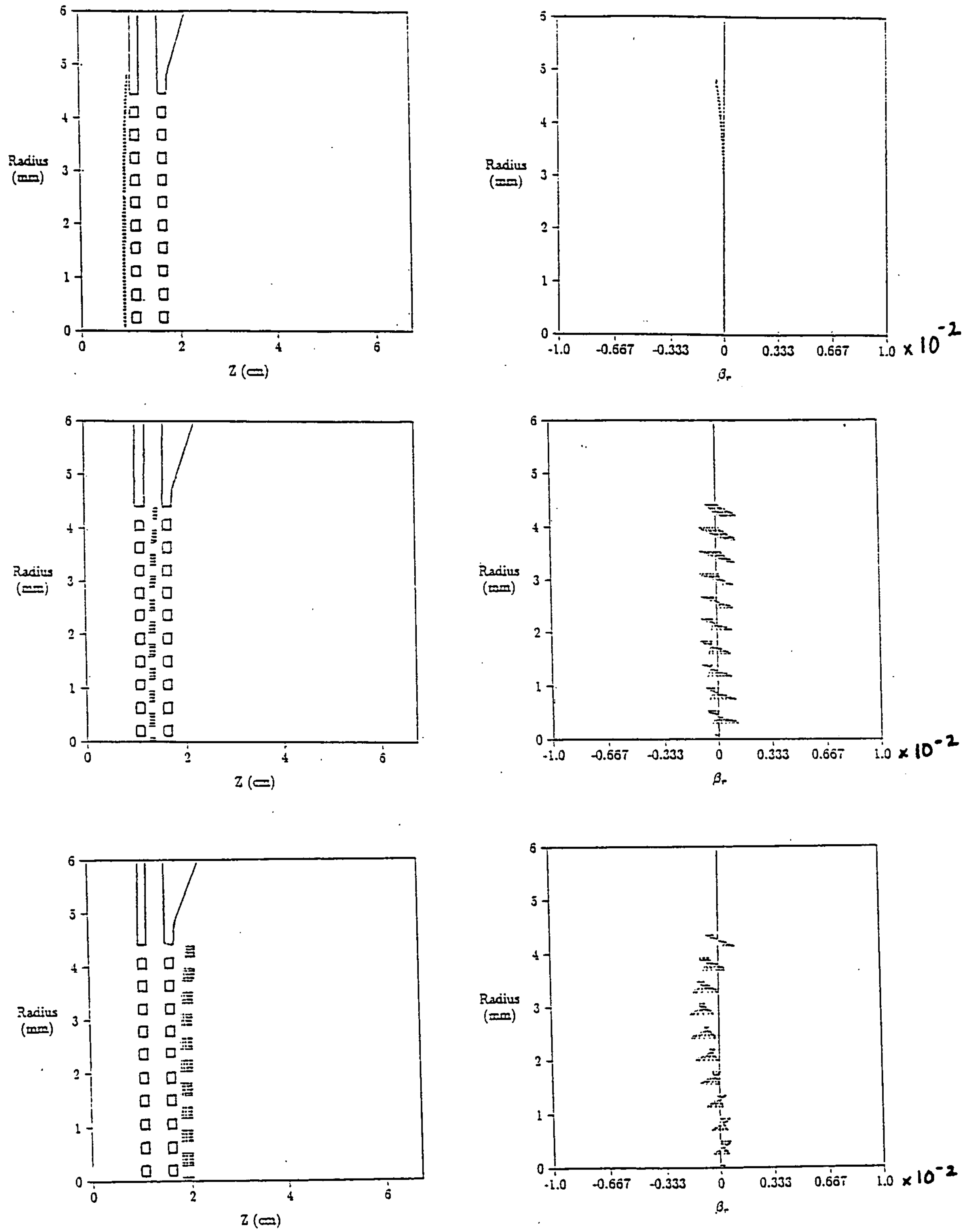

Figure 27: Configuration space and phase space for a solid beam from the simulations. This shows the emittance growth up to the first grid, from the first grid, and from the second grid.

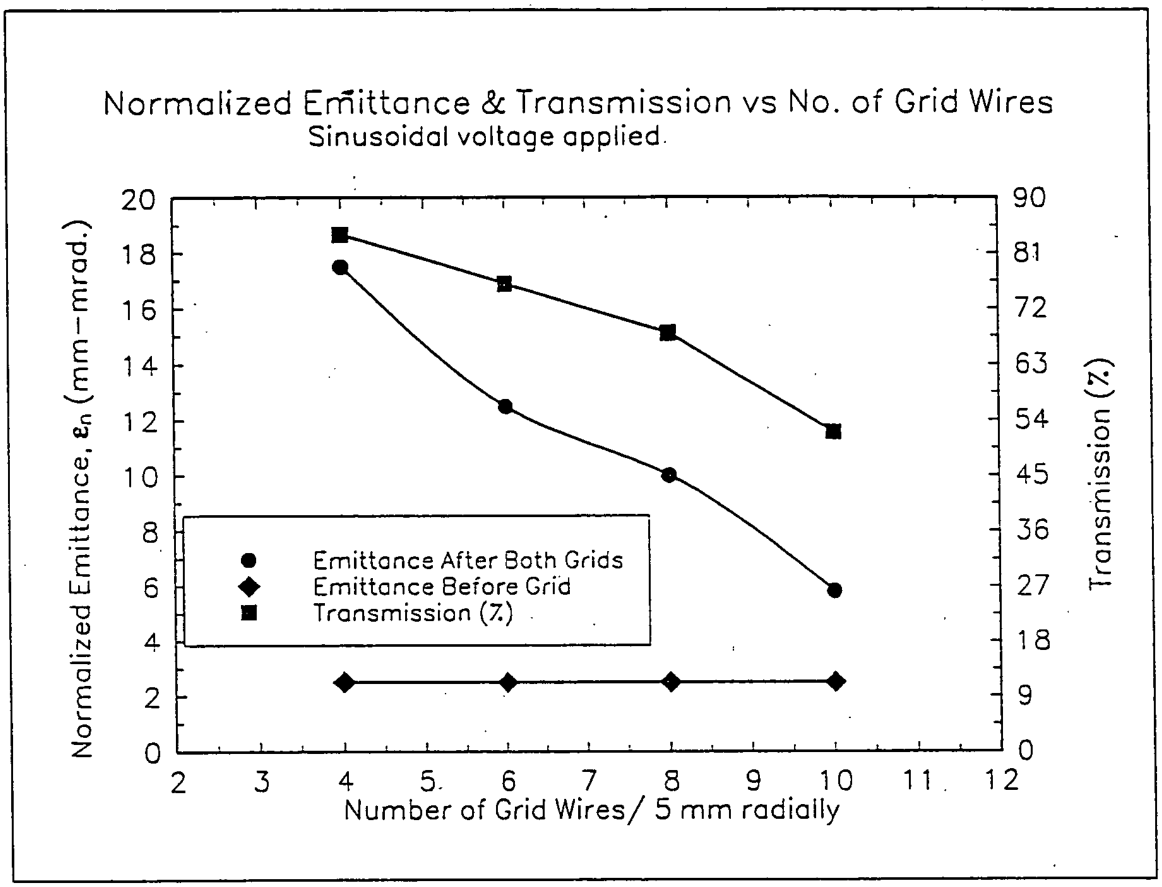

Figure 28: Normalized emmitance and transmission versus number of grid wires with an *ac voltage* applied to the cavity. Grid wire radius is 0.09615 mm.

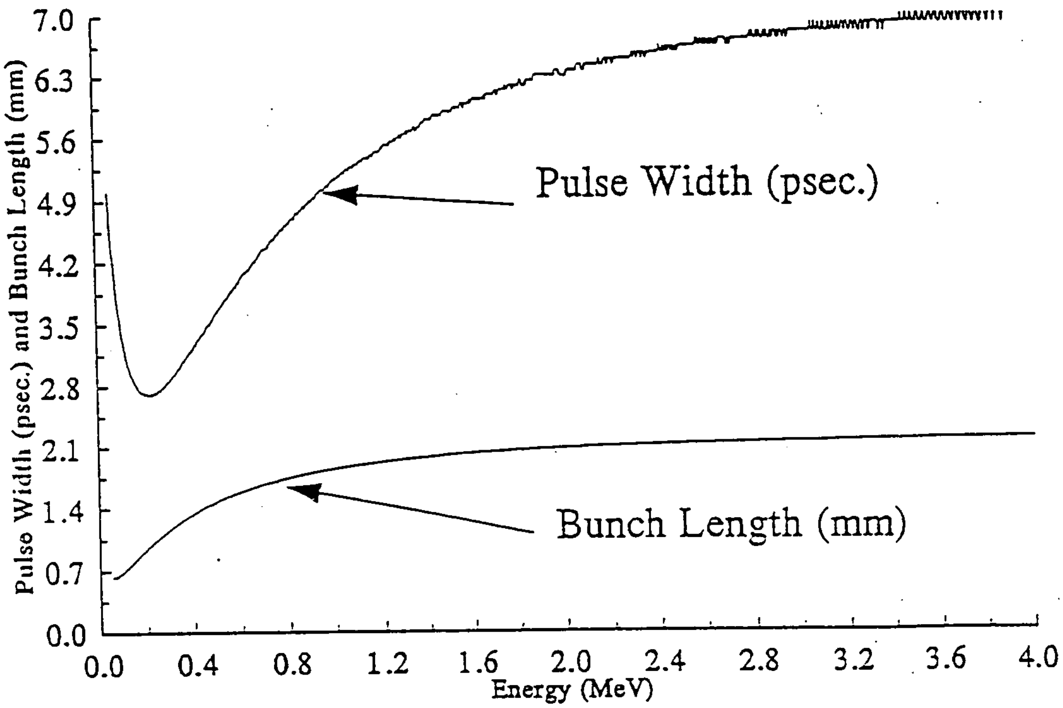

Figure 29: Expansion of micro-pulse from space charge during acceleration, neglecting energy spread. The acceleration field is 20 MV/m and the axial space charge electric field is 2.9 MV/m (corresponding to about 100 nC/cm^3). The initial pulse width is 5 ps at an initial energy of 50 keV.

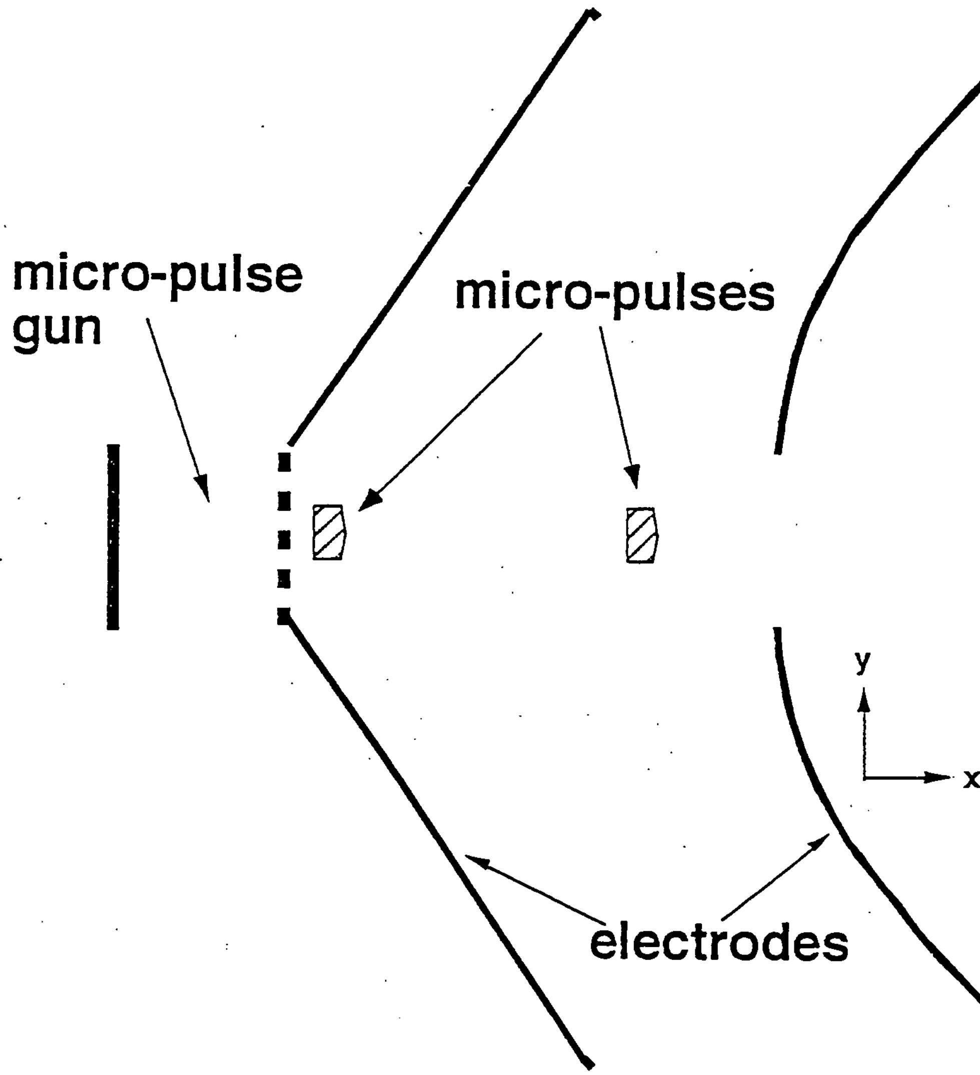

Figure 30: Schematic drawing of a set of electrode shapes for a high-power diode using the modified formulas to the usual Pierce shapes as discussed in the text.

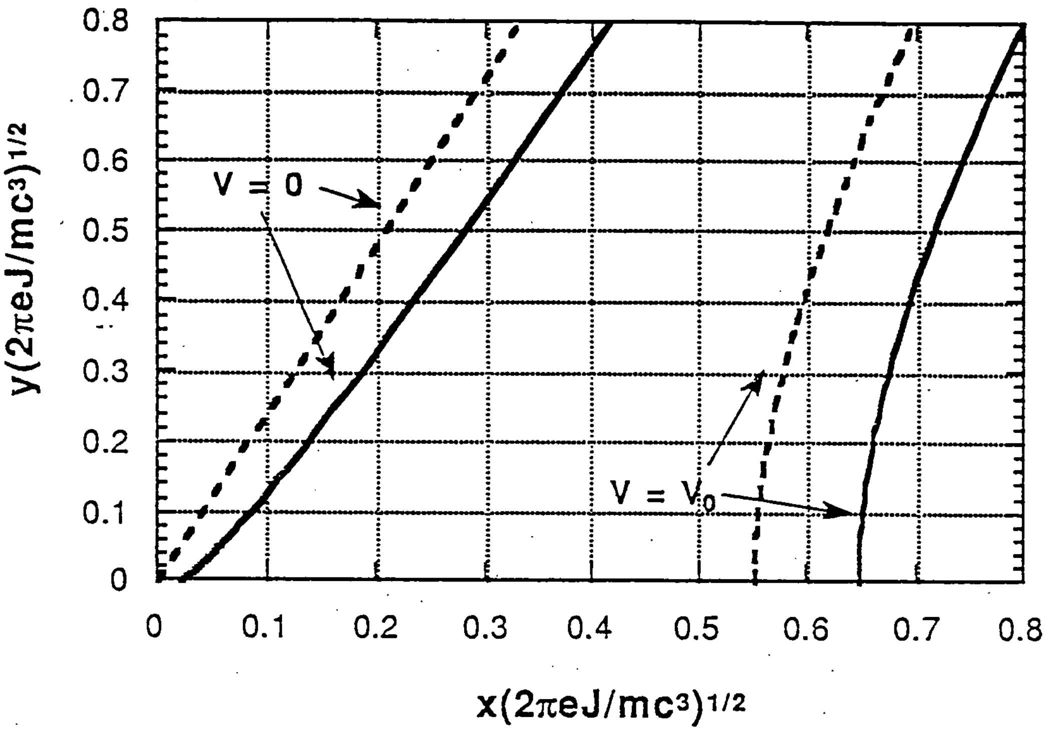

Figure 31: Plot of electrode shapes for a non-space-charge-limited 0.5 MeV diode. The modified shapes [solid lines] and the classical Pierce shapes [broken lines] are shown for comparison. The value of the electric field E_0 at the cathode is such that the quantity ν = 2

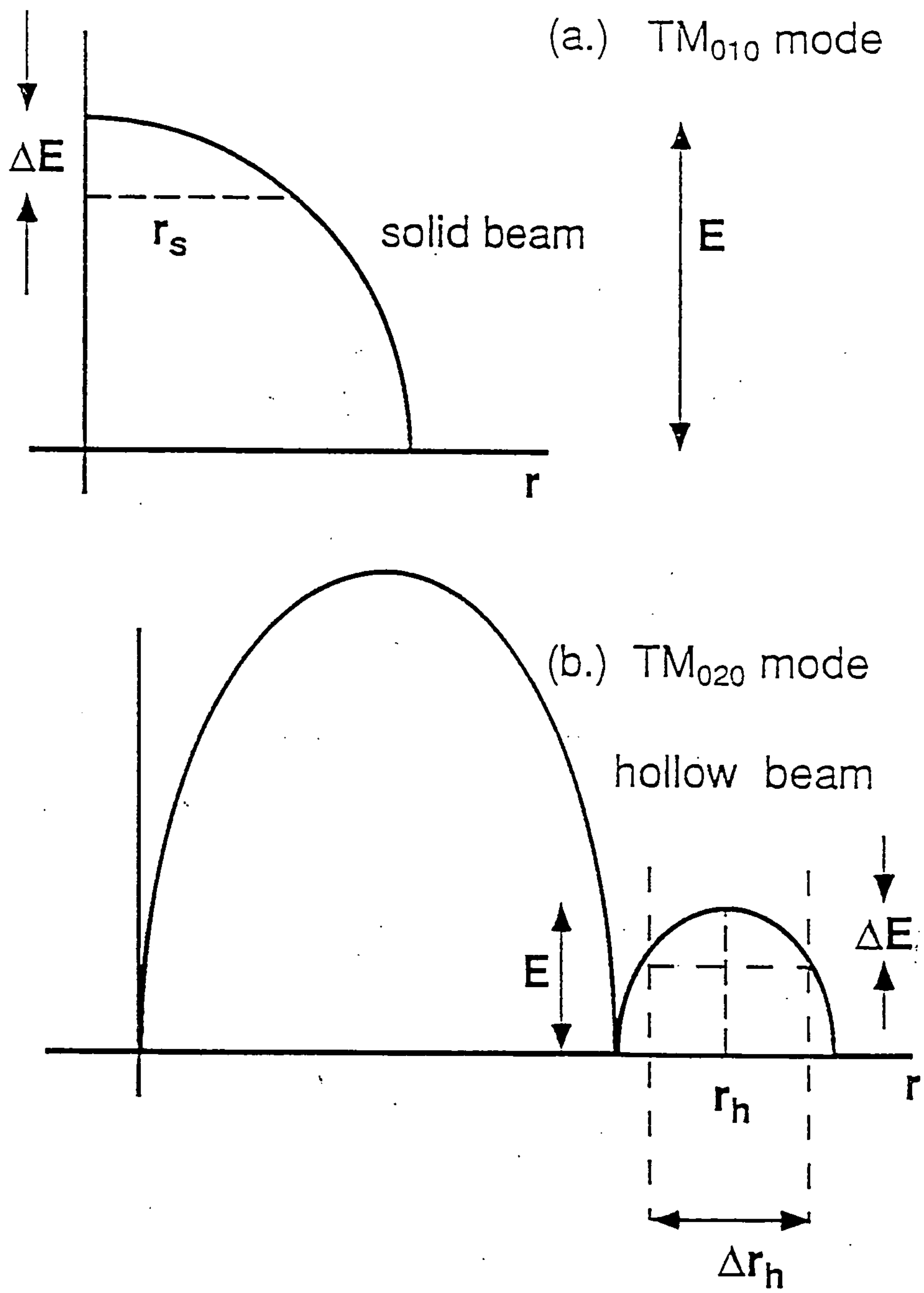

Figure 32: Schematic drawing of emission area and energy spread for a micropulse.

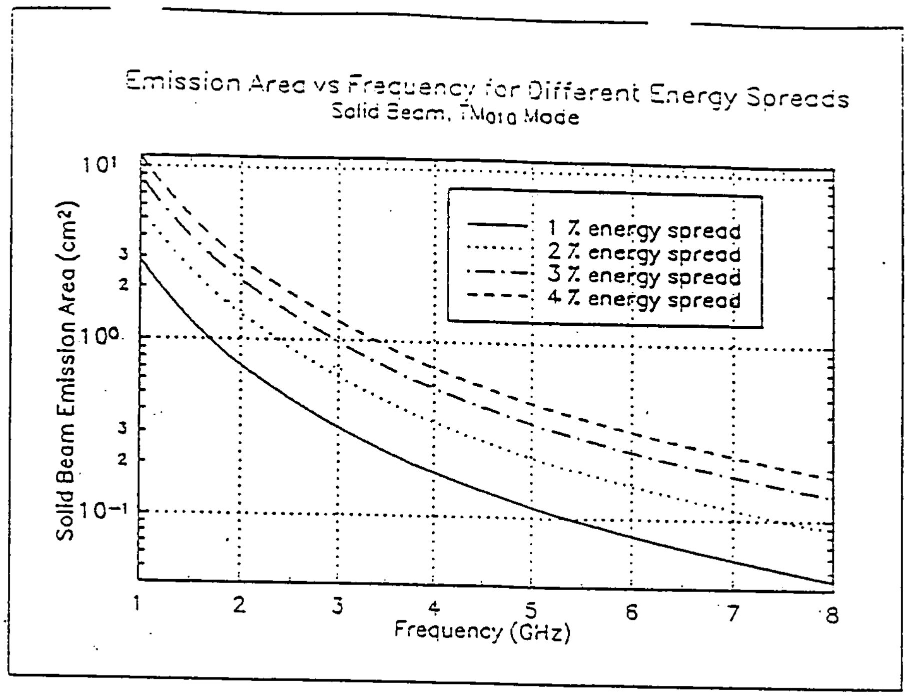

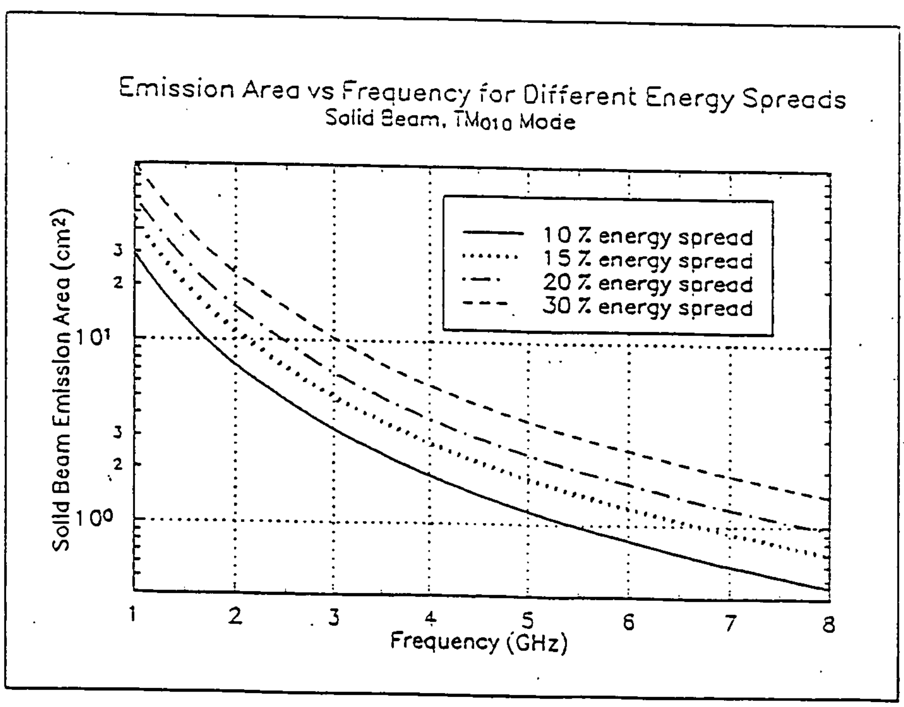

Figure 33: Emission area for a solid beam vs. frequency for different energy spreads (top) 1%-4% energy spread; (bottom) 10%-30% energy spread.

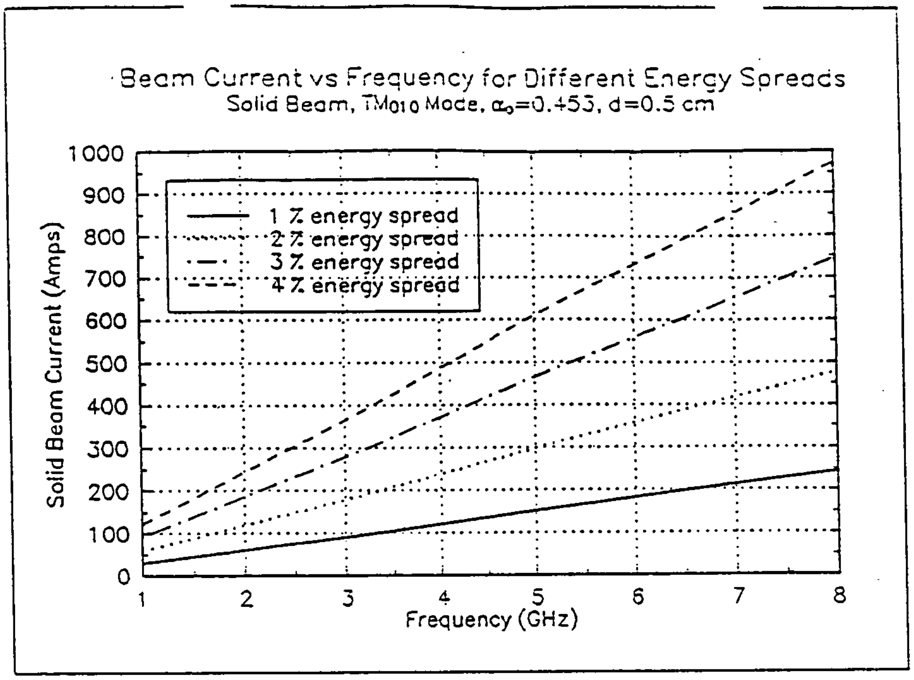

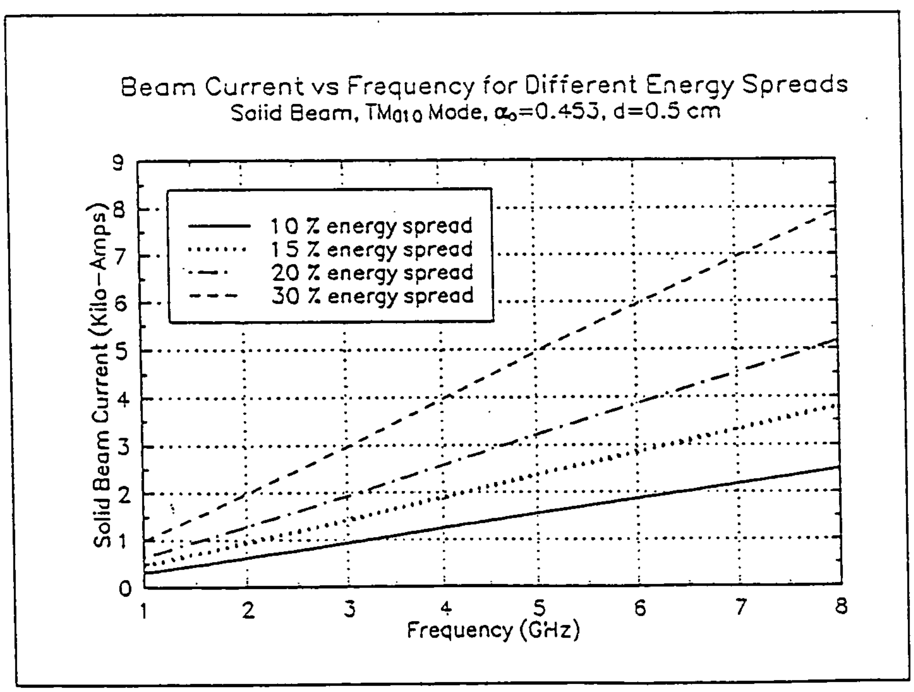

Figure 34: Beam current (solid beam) vs. frequency for different energy spreads and a gap of 0.5 cm.

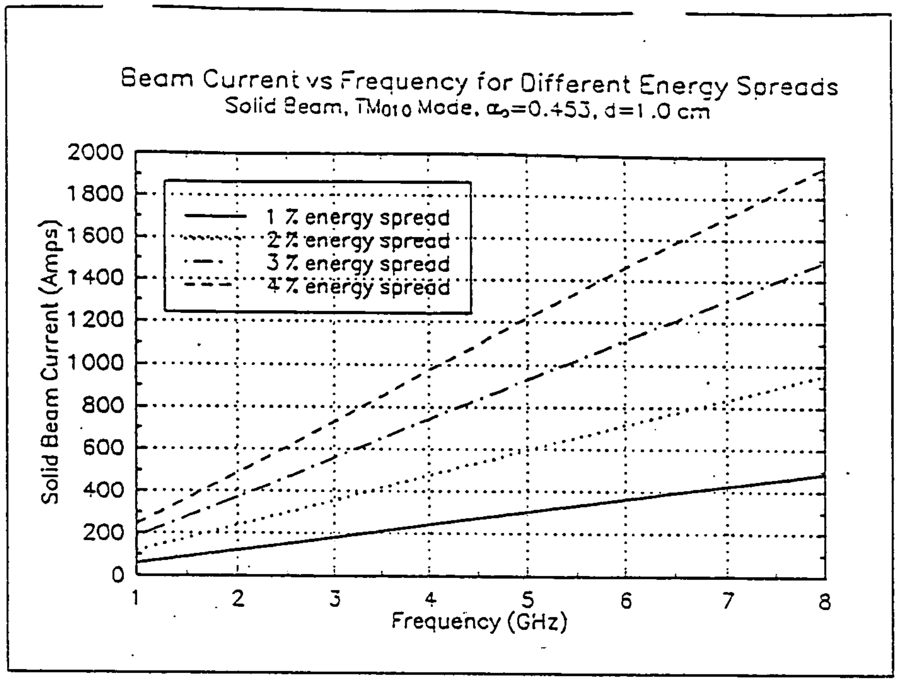

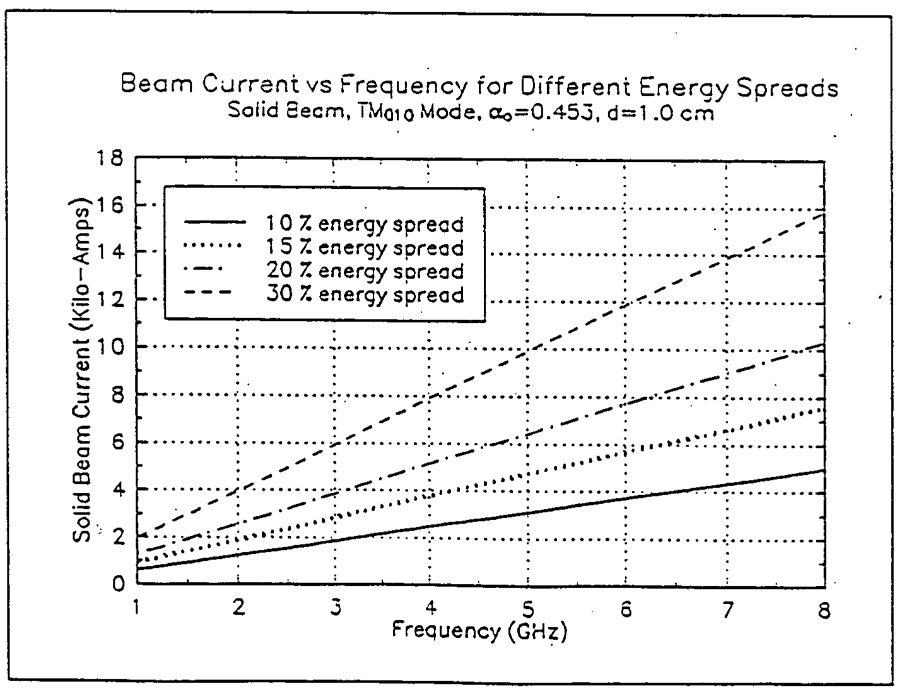

Figure 35: Beam current (solid beam) vs. frequency for different energy spreads and a gap of 1.0 cm.

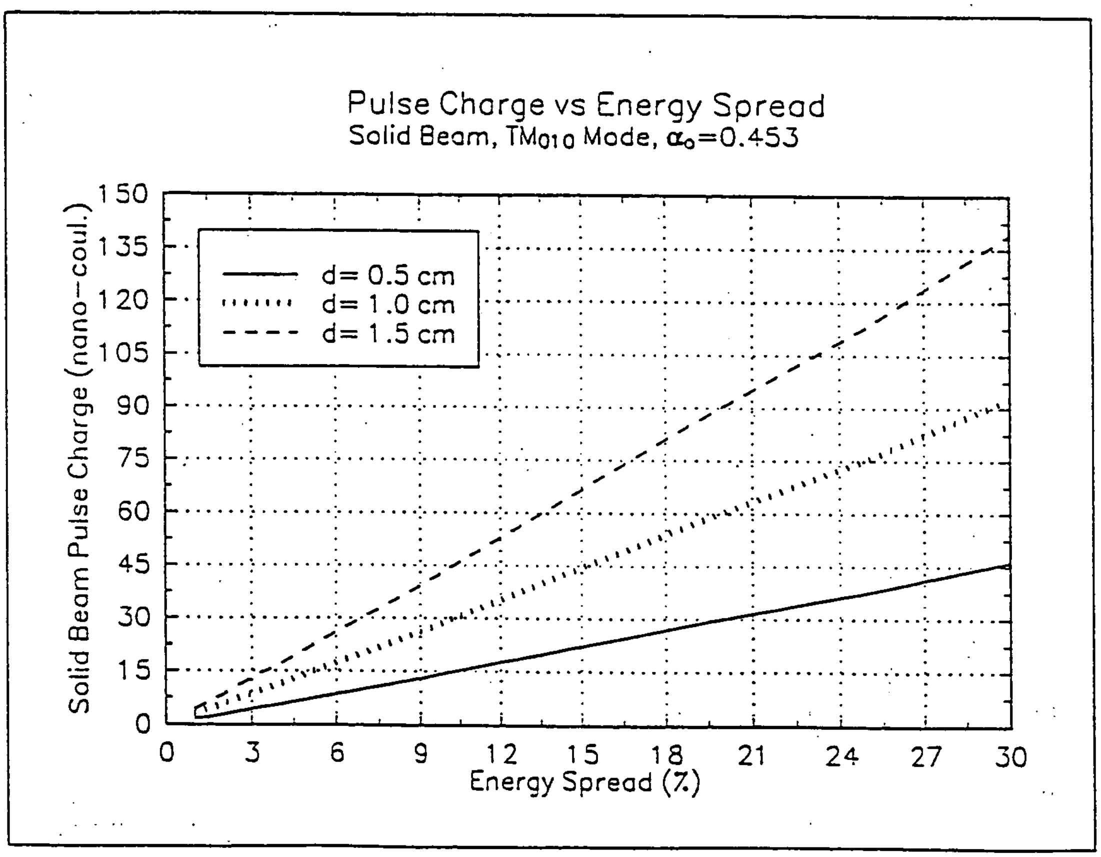

Figure 36: Charge per pulse for a solid beam vs. energy spread.

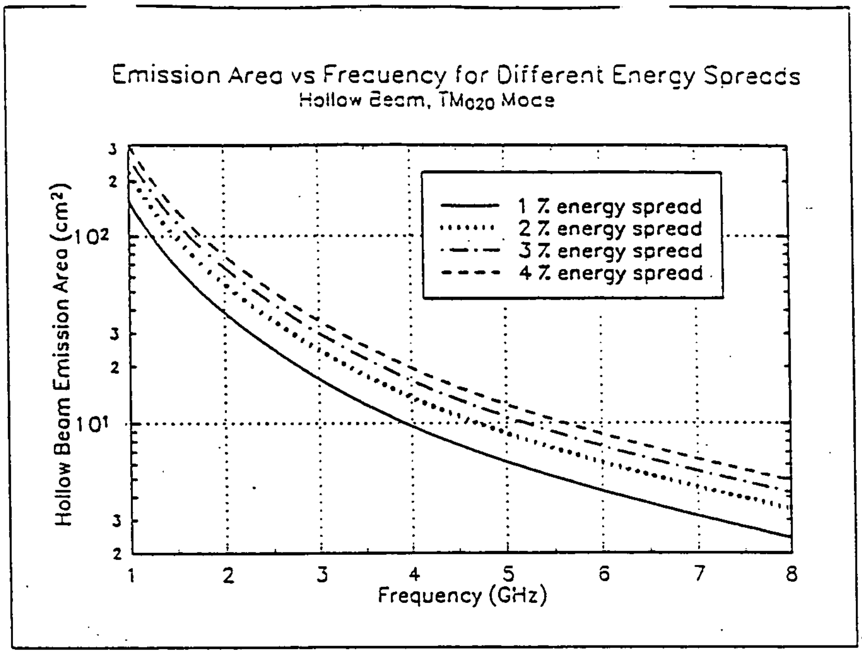

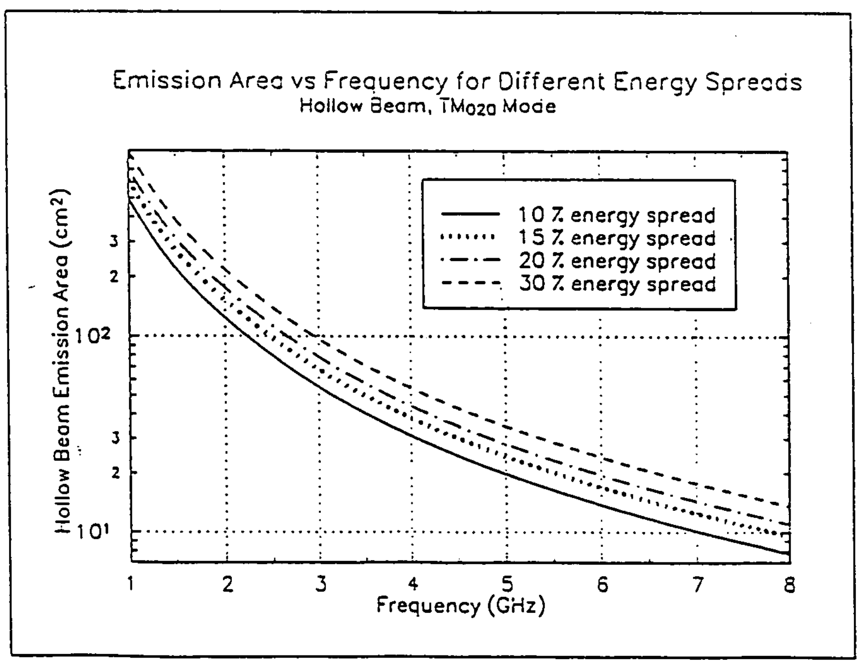

Figure 37: Emission area vs. frequency for different energy spreads. Hollow beam.

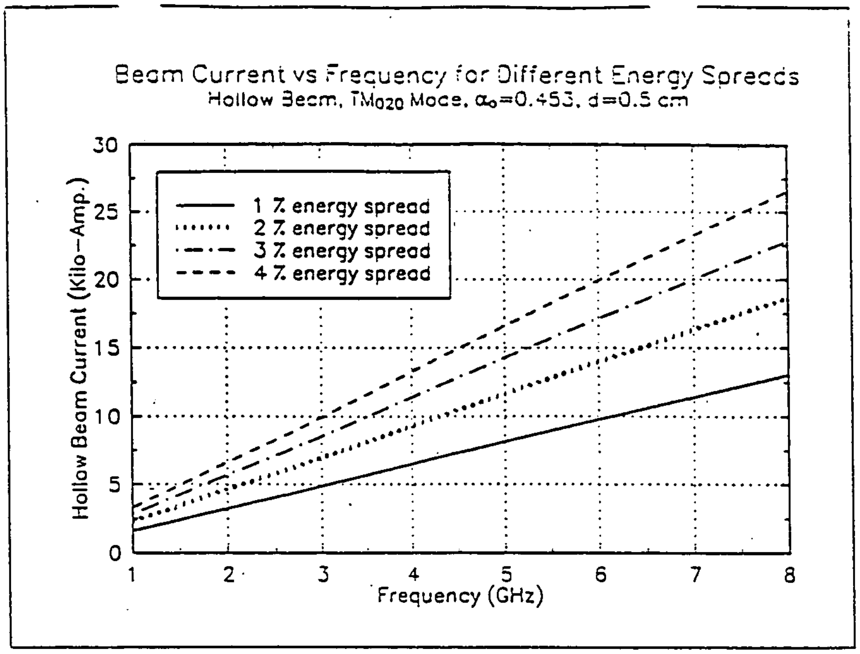

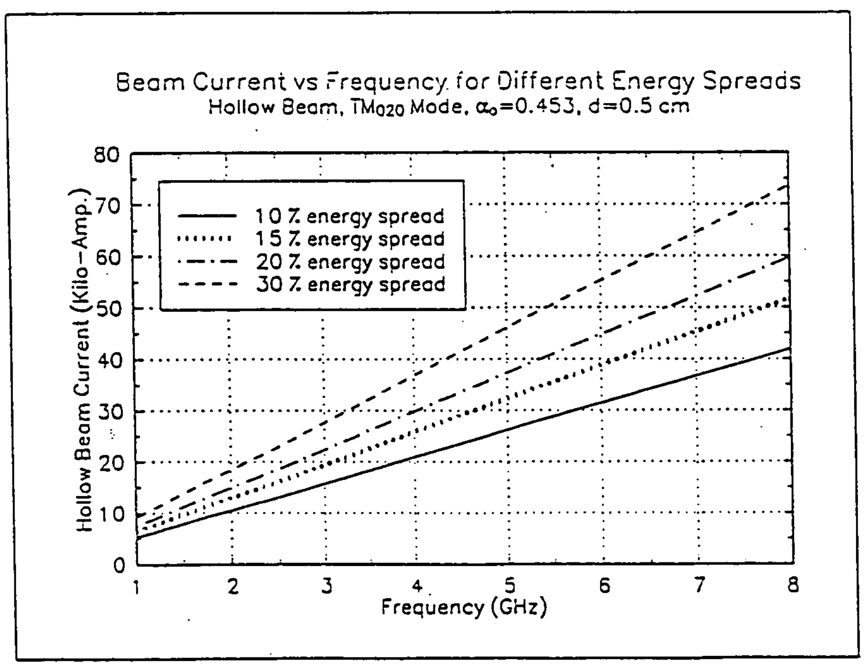

Figure 38: Beam current vs. frequency for different energy spreads. Hollow beam, and $d = 0.5$ cm.

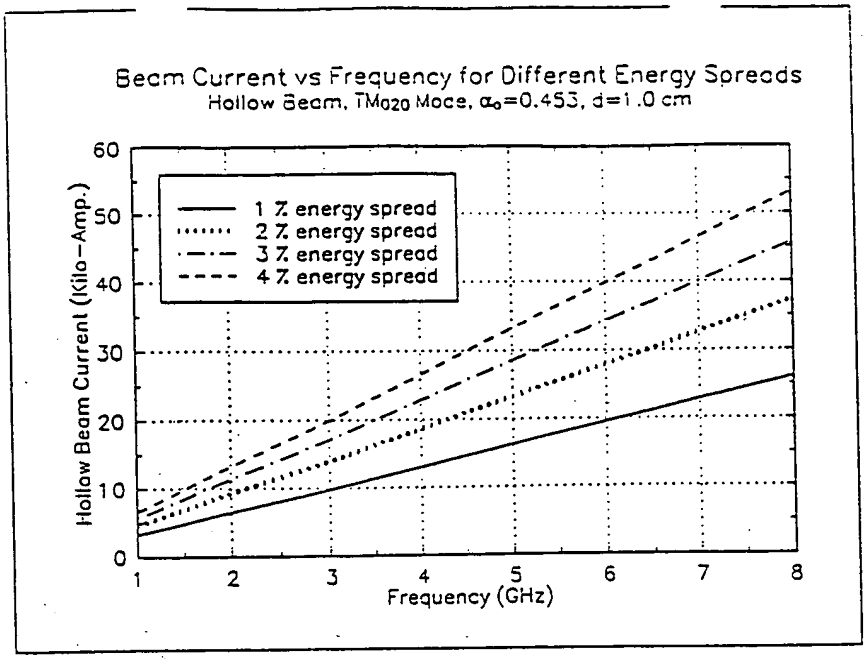

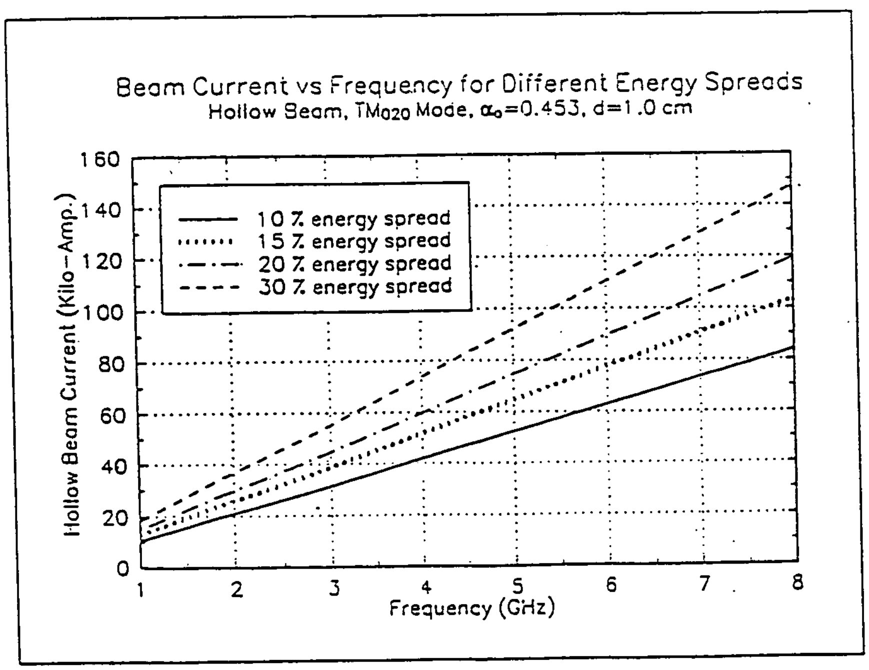

Figure 39: Beam current vs. frequency for different energy spreads. Hollow beam, and $d = 1.0$ cm.

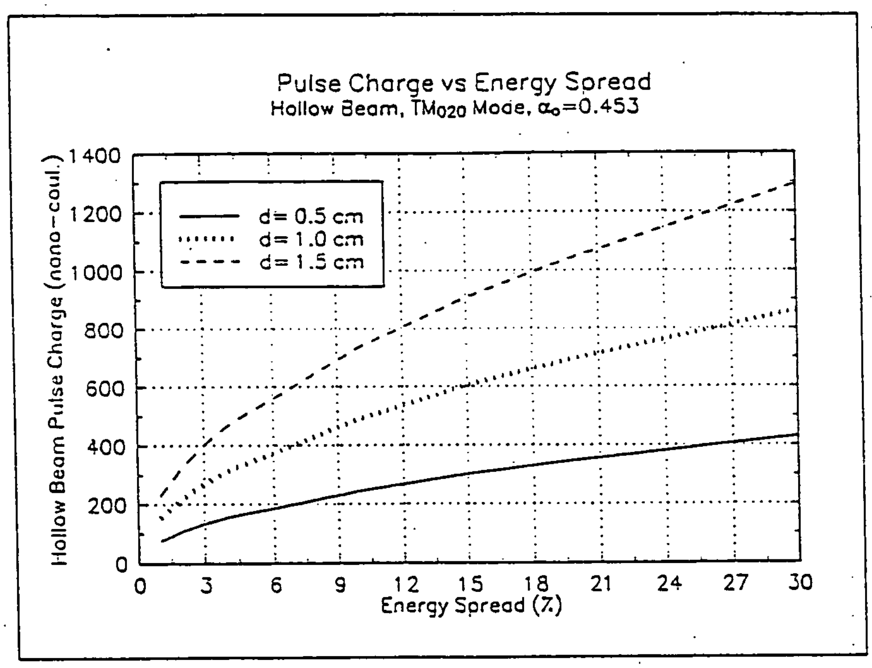

Figure 40: Pulse charge vs. energy spread for hollow beam.

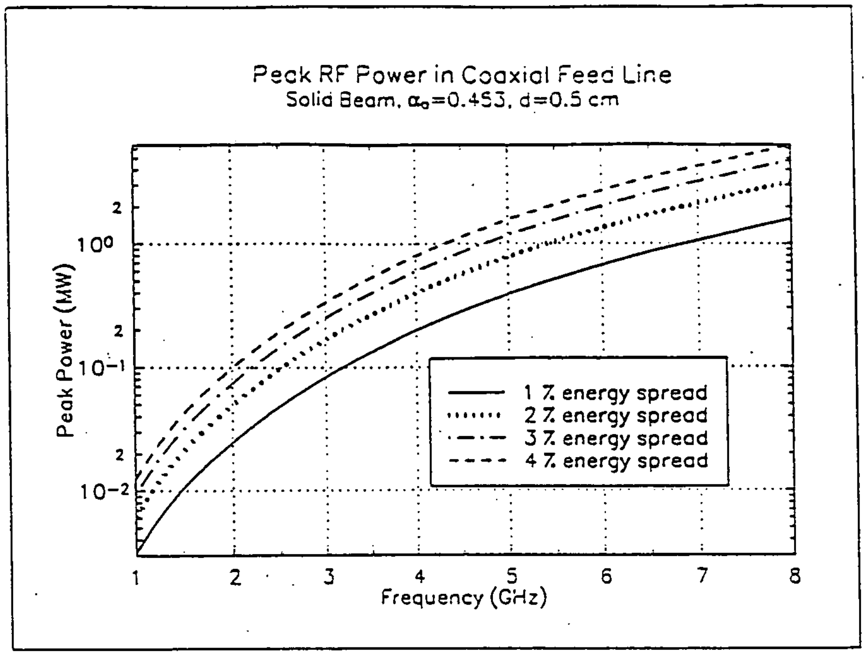

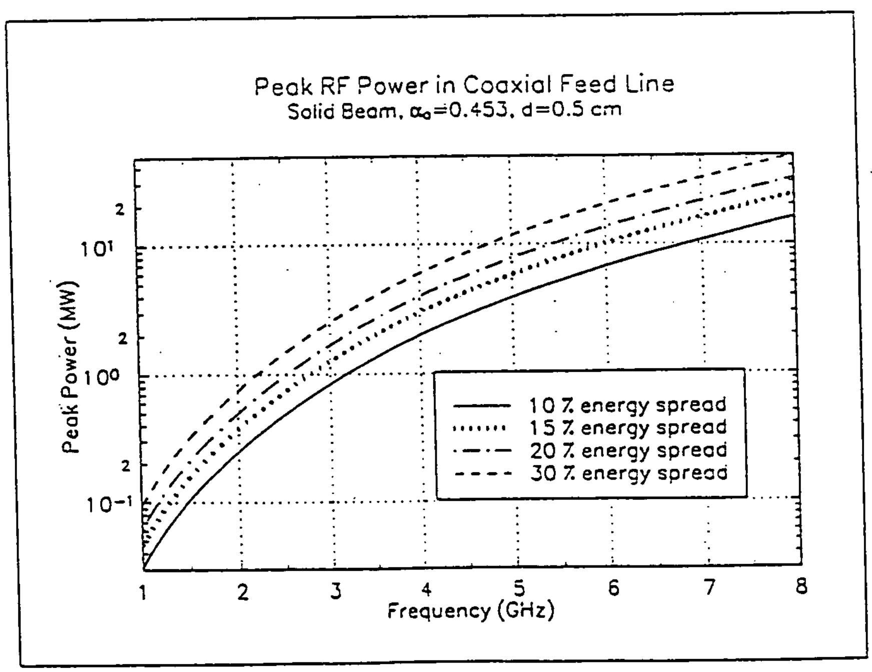

Figure 41: Peak rf power in coaxial feed line for a solid beam, $d = 0.5$ cm.

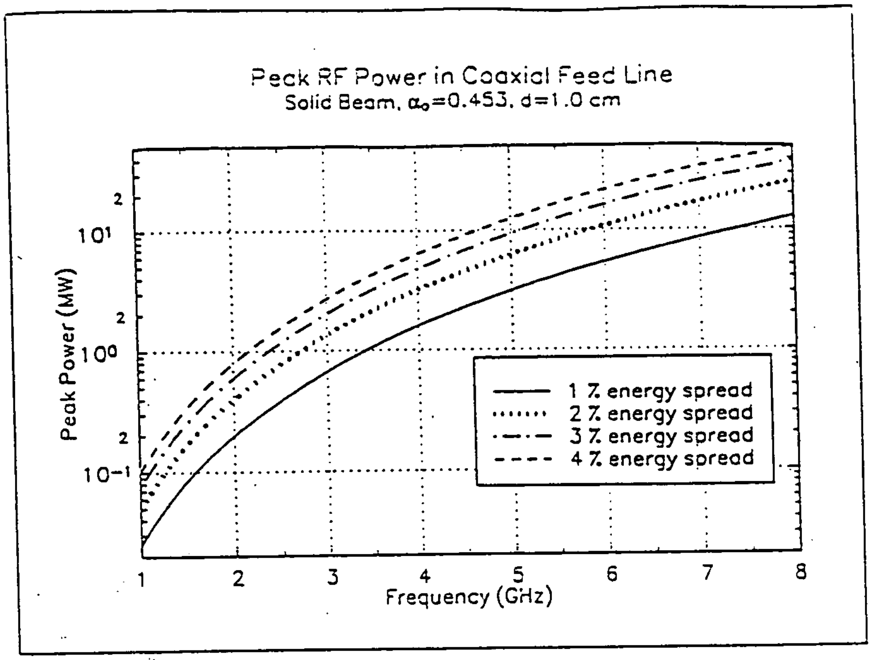

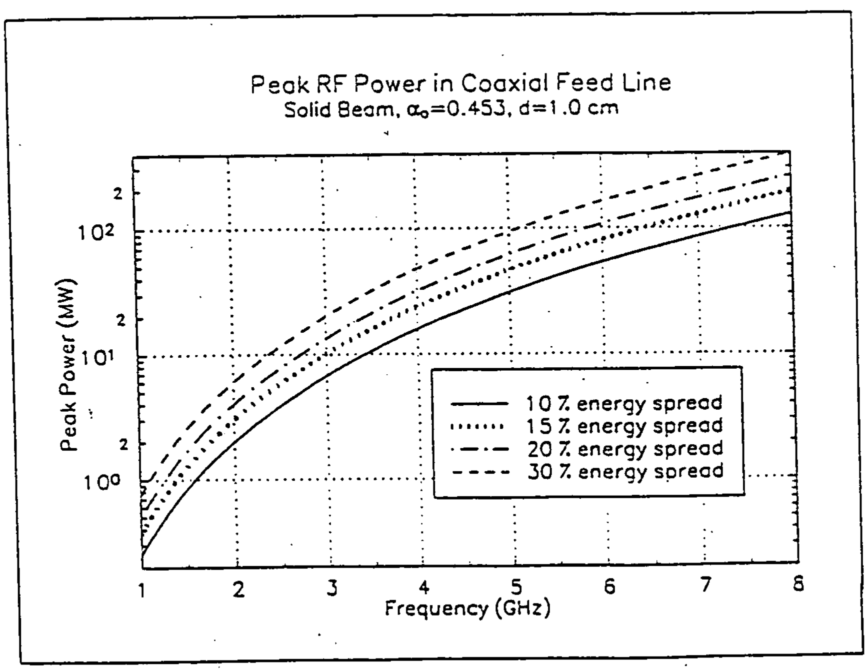

Figure 42: Peak rf power in coaxial feed line for a solid beam, $d = 1.0$ cm.

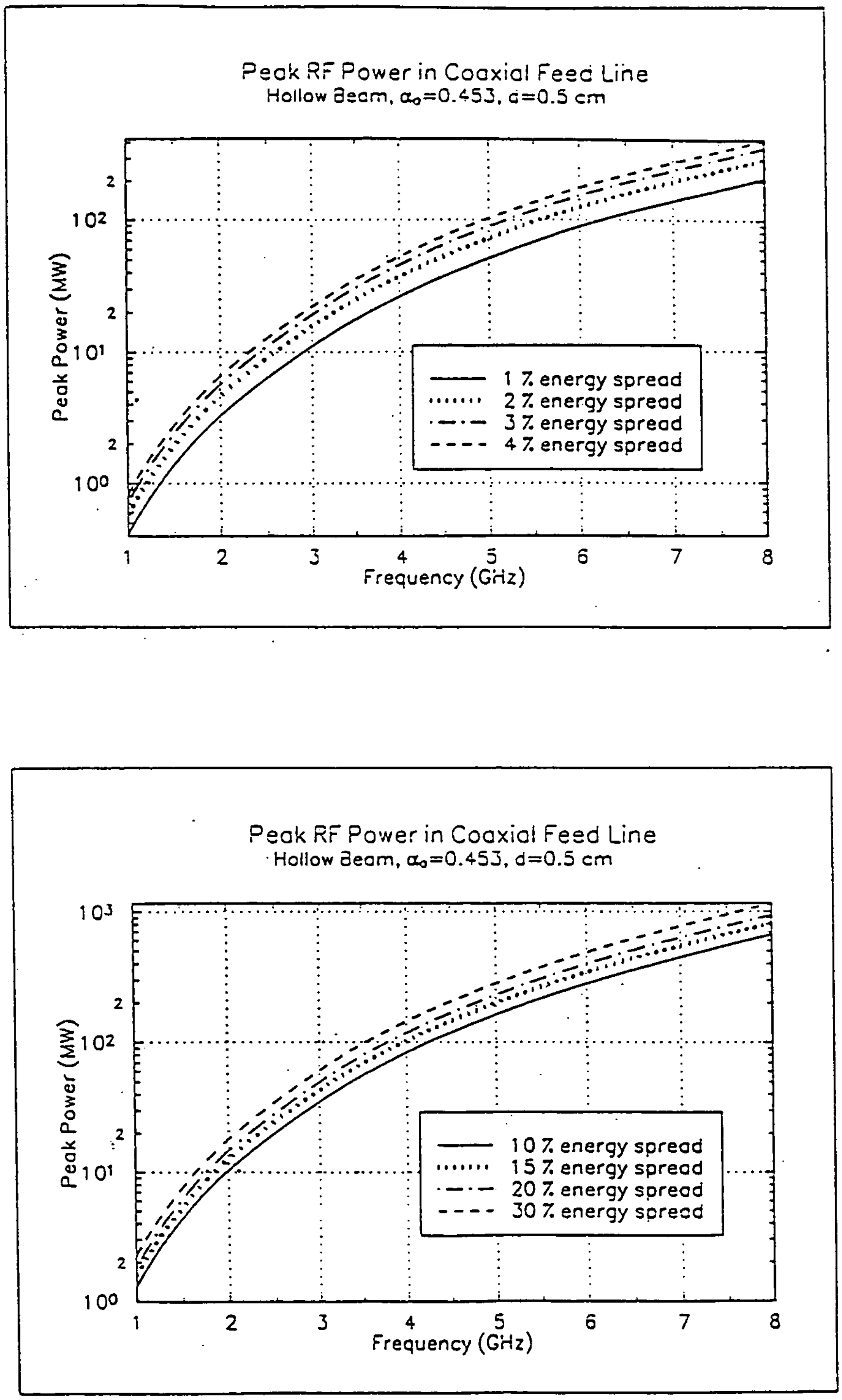

Figure 43: Peak rf power in coaxial feed line for a solid beam, $d = 0.5$ cm.

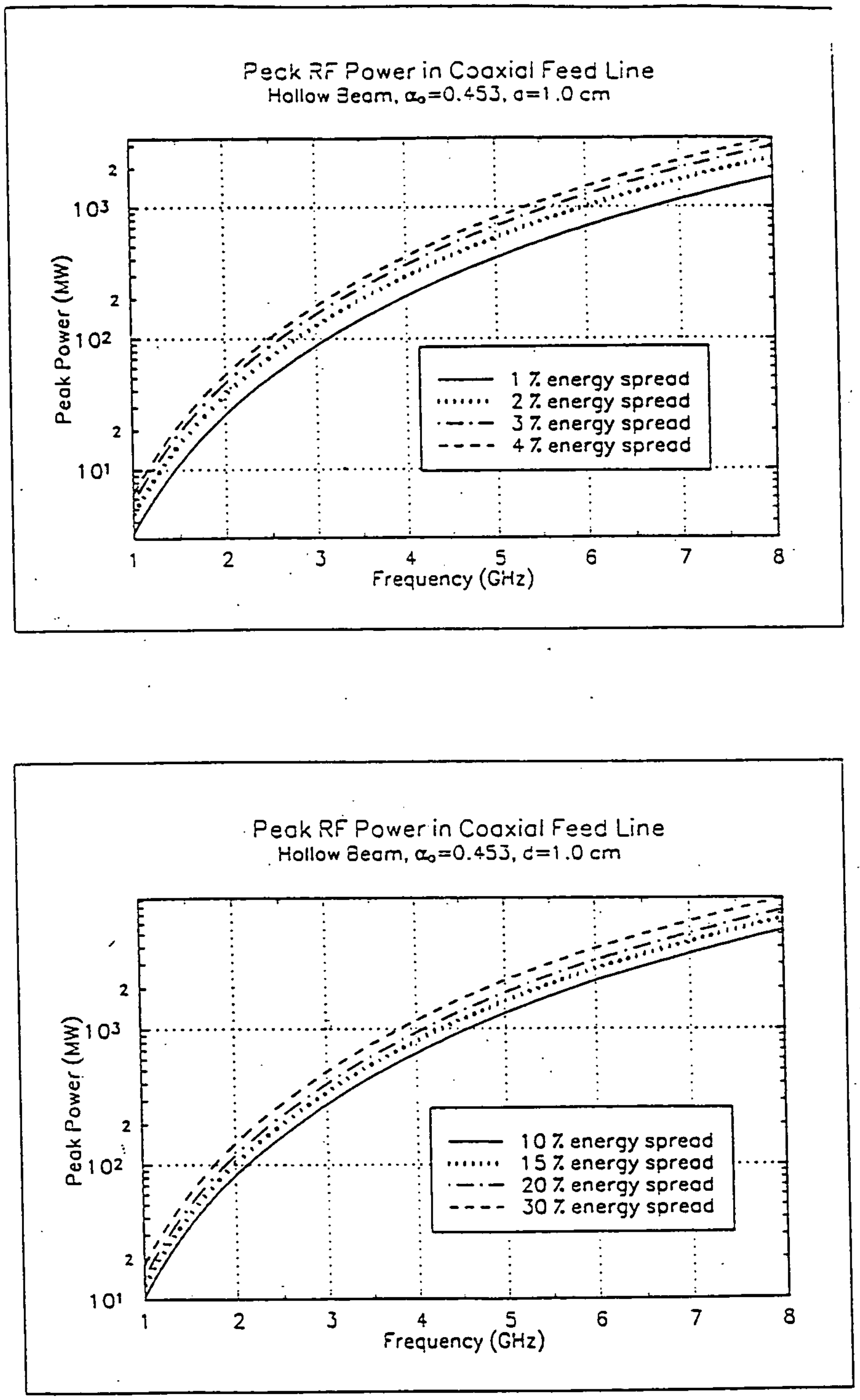

Figure 44: Peak rf power in coaxial feed line for a solid beam, $d = 1.0$ cm.

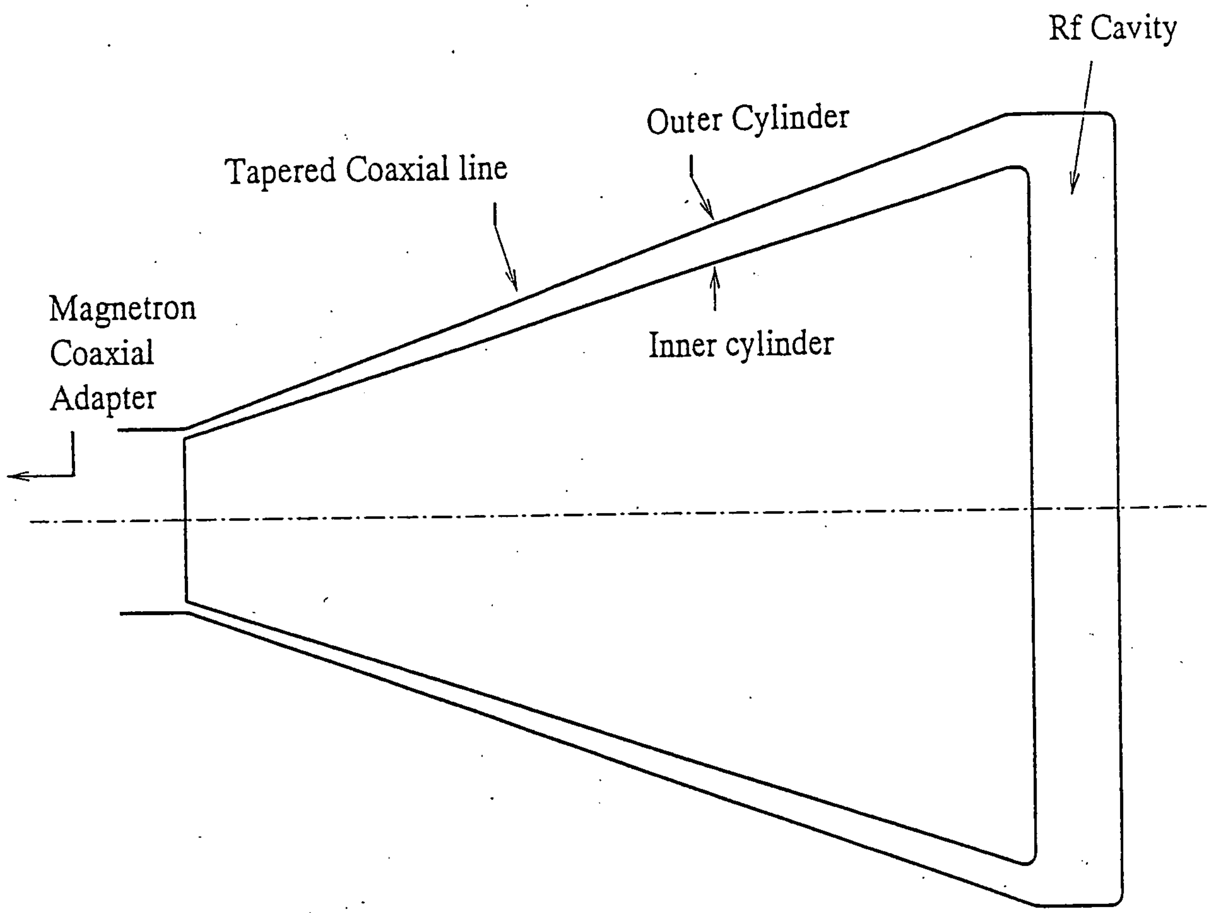

Figure 45: A magnetron feeding energy into the rf cavity. For simplicity a constant, low impedance, coaxial feed line is assumed. Voltage step-up occurs in the rf cavity.

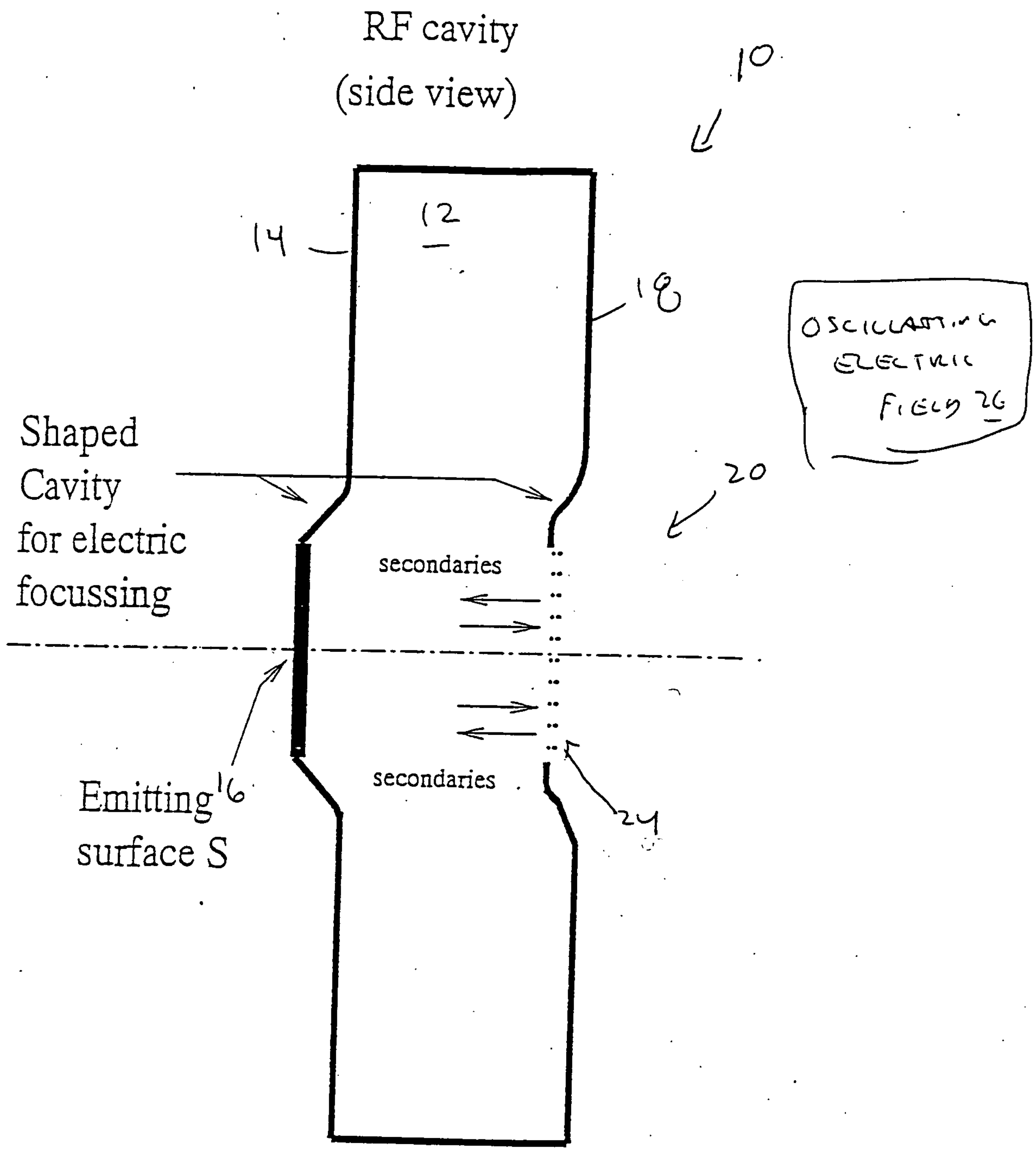

Figure 46: Schematic drawing of a possible design for electrostatic focusing in the MPG.